

The structure of protostellar envelopes derived from submillimeter continuum images

Claire J. Chandler

and

John S. Richer

Department of Physics, University of Cambridge, Cavendish Laboratory, Madingley Road,
Cambridge CB3 0HE, United Kingdom

E-mail: cjc@mrao.cam.ac.uk, jsr@mrao.cam.ac.uk

ABSTRACT

High dynamic range imaging of submillimeter dust emission from the envelopes of eight young protostars in the Taurus and Perseus star-forming regions has been carried out using the SCUBA submillimeter camera on the James Clerk Maxwell Telescope. Good correspondence between the spectral classifications of the protostars and the spatial distributions of their dust emission is observed, in the sense that those with cooler spectral energy distributions also have a larger fraction of the submillimeter flux originating in an extended envelope compared with a disk. This results from the cool sources having more massive envelopes rather than warm sources having larger disks. Azimuthally-averaged radial profiles of the dust emission are used to derive the power-law index of the envelope density distributions, p (defined by $\rho \propto r^{-p}$), and most of the sources are found to have values of p consistent with those predicted by models of cloud collapse. However, the youngest protostars in our sample, L1527 and HH211-mm, deviate significantly from the theoretical predictions, exhibiting values of p somewhat lower than can be accounted for by existing models. For L1527 heating of the envelope by shocks where the outflow impinges on the surrounding medium may explain our result. For HH211-mm another explanation is needed, and one possibility is that a shallow density profile is being maintained in the outer envelope by magnetic fields and/or turbulence. If this is the case star formation must be determined by the rate at which the support is lost from the cloud, rather than the hydrodynamical properties of the envelope, such as the sound speed.

Subject headings: Circumstellar matter — stars: formation — ISM: clouds — dust, extinction

1. Introduction

One of the fundamental problems associated with assembling an observationally-based framework for early protostellar evolution is that the photospheres of deeply-embedded protostars are highly obscured, and the techniques used for establishing the properties of optically-visible young stellar objects, such as comparison with model isochrones in the Hertzsprung-Russell diagram, are not available. Instead, we are limited to measuring only (1) the interaction of the protostar with the surrounding molecular cloud, and (2) the luminosity of the protostar/disk system embedded at the center. Neither of these can provide a value for the mass, radius, or age of the protostar directly, without making several assumptions of how the central mass is being accumulated as a function of time. For example, one possible measure of the age of a protostar may be the dynamical age of its outflow, but it is hard to tie this to the actual age of the protostar without knowing exactly when the mass loss began, or exactly how the outflow propagates through the interstellar medium. Similarly, the bolometric luminosity, L_{bol} , has been used to infer protostellar ages (Barsony 1994), by assuming it derives entirely from accretion so that $L_{\text{bol}} = GM_*(t)\dot{M}/R_*$, where \dot{M} is the accretion rate, the stellar mass $M_*(t) = \int \dot{M} dt$, and R_* is the (assumed) stellar radius. The protostellar age is then approximately $M_*(t)/\dot{M} = L_{\text{bol}}R_*/G\dot{M}^2$, which will clearly depend upon how \dot{M} evolves with time.

Predictions for $\dot{M}(t)$ during cloud collapse vary dramatically, and depend upon the initial density distribution within the cloud. The model most commonly cited in the literature is the self-similar solution for the collapse of a singular isothermal sphere (SIS), which is based on the work of Shu (1977) and subsequent refinements to include slow rotation (Terebey, Shu, & Cassen 1984). In this model collapse begins in a sphere with a density distribution $\rho \propto r^{-2}$ at all radii. Such a configuration is highly unstable, and if perturbed, a region of free-fall collapse spreads outwards from the center at the local sound speed, a . The rate at which material arrives at the hydrostatic protostar forming at the center of the collapse flow is therefore constant, with a value $\dot{M} \sim a^3/G$, where G is the gravitational constant. On the other hand, self-similar solutions for isothermal collapse beginning from unstable configurations with density distributions flatter than the SIS have time-varying accretion rates which can peak at approximately fifty times the Shu value, declining thereafter (Larson 1969; Penston 1969; Hunter 1977; Whitworth & Summers 1985). Numerical hydrodynamical simulations show results similar to those described by the analytic solutions (Foster & Chevalier 1993).

The dependence of \dot{M} on the initial conditions from which collapse begins is clearly extremely important for the subsequent evolution of L_{bol} and M_* , affecting the numbers of protostars detectable in a given stage of evolution, and their derived statistical lifetimes. Unfortunately, independent measures of $\dot{M}(t)$ are not available for deeply-embedded protostars, but the models do suggest other means of discriminating between the various possibilities for

early protostellar evolution and cloud collapse. After a hydrostatic protostar has formed at the centre of a cloud core, the density distribution within the surrounding cloud also depends on the initial conditions of the collapse. In the extreme case of the collapse of a SIS, material is stationary and the density distribution remains proportional to r^{-2} outside the expanding region of infall, while directly inside the expansion wave it becomes r^{-1} , steepening again to $r^{-3/2}$ as free fall is established (Shu 1977). For collapse initiated from flatter density distributions the outer parts of the cloud also have $\rho \propto r^{-2}$, but are already moving inwards, and match smoothly to an expanding region of free fall having $\rho \propto r^{-3/2}$ (Whitworth & Summers 1985; Foster & Chevalier 1993). These models therefore suggest two potential observational tests of the initial conditions, those of measuring the radial density profiles of cloud cores and protostellar envelopes, and of determining the velocity distribution to establish whether the outer parts are static or infalling. This latter test is particularly difficult once a protostar has already formed, because outflow and multiple velocity components along the line of sight confuse the interpretation of spectral line emission. Perhaps more promising as an initial test of the collapse models is the measurement of radial density profiles, particularly taking advantage of the simple radiative transfer of millimeter and submillimeter dust emission. This technique has been successfully used for establishing that the density profiles of starless cores are somewhat flattened within a radius of approximately 4000 AU, having $\rho \propto r^{-1.2}$ rather than the r^{-2} of the SIS (Ward-Thompson et al. 1994; André, Ward-Thompson, & Motte 1996).

Once a dense core has lost all means of support and has begun to collapse, and a hydrostatic protostar has formed at the center, then the density profile in the surrounding envelope should be between $r^{-3/2}$ and r^{-2} for initial conditions comprising non-singular isothermal spheres in unstable hydrostatic equilibria. Indeed, in this picture, we would expect to detect an evolution from r^{-2} in the envelopes of the youngest (Class 0) protostars to the more shallow $r^{-3/2}$ in older sources. For cloud cores which are initially sufficiently centrally condensed the numerical simulations of Foster & Chevalier (1993) suggest that at late times the hydrodynamics of the collapse resembles the Shu solution. In this case, the evolution of the density profile might be more complicated, starting out with r^{-2} , and moving through a somewhat flatter ($\rho \propto r^{-1}$) phase until $r^{-3/2}$ dominates. For the few objects which have been studied to date, the results remain confusing. Some sources do show the $r^{-3/2}$ consistent with free-fall collapse (e.g., B335: Chandler & Sargent 1993), but others seem to exhibit extremely flat profiles, $r^{-0.5}$ (e.g., VLA1623: André, Ward-Thompson, & Barsony 1993). A recent analysis of the shape of far-infrared/millimeter dust spectral energy distributions (SEDs) suggests that r^{-1} may be appropriate for the Class I sources TMC1, TMC1A, and Haro 6-10 in Taurus (Chandler, Barsony, & Moore 1998), and few objects show density profiles as steep as the r^{-2} expected for early times.

The constraints on the density distributions obtained so far have been limited by the poor dynamic range achievable using single-element detectors on submillimeter telescopes.

This situation has been dramatically changed recently by the development of submillimeter array cameras such as the Submillimetre Common-User Bolometer Array (SCUBA) on the James Clerk Maxwell Telescope (JCMT), which finally allows a detailed investigation of the distribution of dust emission from protostellar envelopes, to search for evidence of evolutionary and environmental effects in envelope structure. We have used SCUBA to image the submillimeter dust emission from circumstellar material around eight protostars, four in the Taurus molecular cloud and four in Perseus, and we use the observed intensity profiles to derive density distributions in their envelopes. Submillimeter dust emission is particularly suitable because the envelope emission is optically thin, but a problem arises when considering all possible origins of the dust emission. Even young, deeply embedded protostellar systems are surrounded by circumstellar disks (e.g., Chandler 1998), and this compact component must be separated from the envelope if the structure of the envelope is to be analyzed. This requirement limits somewhat the number of sources for which envelope structure can be studied.

2. Source sample

Since considerable information about both the compact disk component and the geometry of any outflow cavity is required for a full analysis of the observed dust distribution, only well-studied objects have been observed in this current work. This does, of course, produce a highly-biased sample, but is clearly a necessary first step. Eight protostars have been selected, four from the Taurus molecular cloud ($D = 140$ pc: Elias 1978; Kenyon, Dobrzycka, & Hartmann 1994), and four from the Perseus star forming region. The distance to Perseus is uncertain, with estimates ranging from 220 pc (Cernis 1990) to 350 pc (Herbig & Jones 1983) reported in the literature. A distance of 350 pc for all the Perseus sources is assumed in the analysis below, but the effect of using a smaller distance on the final results is also investigated. The sources cover a range of spectral class and luminosity (Table 1), and their outflow directions, opening angles, and inclination angles, are all known. The Taurus and Perseus clouds are forming stars in somewhat different modes; the protostars in Taurus are fairly isolated, and are predominantly low-mass, while those in Perseus are more clustered and more luminous (e.g., Ladd, Lada, & Myers 1993). The average temperature of the molecular gas in the Perseus cloud is also a few degrees higher than in Taurus (Ladd, Myers, & Goodman 1994), which translates into a higher sound speed for the gas in Perseus compared with Taurus.

3. Observations

The submillimeter camera SCUBA on the 15-m JCMT on Mauna Kea, Hawaii, comprises two bolometer arrays, a long-wavelength array containing 37 elements optimized for operation in the 850 and 750 μm atmospheric windows, the other a 91-element short-wavelength array with filters at 450 and 350 μm . Combinations of 850/450 μm and 750/350 μm may be observed simultaneously through the use of a dichroic beam splitter. The bolometers are located in a hexagonal pattern, spaced two full beamwidths apart, so the secondary mirror is “jiggled” to produce a fully-sampled image. Further technical details of observing with SCUBA on the JCMT are described by Holland et al. (1999). All eight sources listed in Table 1 were observed at all four wavelengths in 1998 January, using a chop throw of 120 arcsec and a chop frequency of 7.8 Hz. The chop direction for each source was chosen to avoid both the outflow and possible envelope emission perpendicular to the outflow. L1551 IRS5 and TMC1A were also observed at 850 μm , with a chop throw 120 arcsec in azimuth, in service mode in 1997 July and August. The atmospheric transmission was monitored by performing sky dips at regular intervals, which, combined with measurements of the 225 GHz opacity obtained from the tipping radiometer located at the Caltech Submillimeter Observatory (CSO), allowed a conversion factor from $\tau_{225 \text{ GHz}}$ to τ_λ to be determined. The absolute flux scale was established from observations of Uranus, Mars, Saturn, NGC2071, and CRL618 (Sandell 1994, 1998), and the pointing and focus were checked regularly using calibrators near our program sources. SCUBA’s 1.3 mm photometric pixel was also used to make a strip scan perpendicular to the outflow for each object. The uncertainty in the absolute flux calibration at 1.3 mm, 850, 750, 450, and 350 μm is 6, 8, 13, 20 and 30% respectively.

SCUBA is located at a Nasmyth focus of the JCMT, without a beam rotator, and images in equatorial coordinates have been produced using a Gaussian interpolation function. The arrays contained several noisy or bad bolometers, which have been removed from the data. To avoid obtaining holes in the resulting images an individual source was typically observed with between four and seven different position offsets, and the data co-added in the final stages of the data reduction after aligning the peaks in each separate image. Shifts of less than 2 arcsec were applied during the alignment process, but this technique ensured that pointing offsets between different integrations were minimized. The typical rms noise achieved at 850 μm was 20 mJy beam⁻¹, and at 450 μm was 150 mJy beam⁻¹.

The beam was measured at each wavelength by imaging Uranus (in 1997) and Mars (in 1998), both of which had disk diameters of approximately 4 arcsec at the time of observation. The images of Mars at 850, 750, 450 and 350 μm are shown in Fig. 1. They illustrate that the beam is elongated in the chop direction, even at 850 μm , although it is the wavelength least affected by this problem. They also show significant power in the error beam, especially at the

short wavelengths. Because the images of the program sources were combinations of several integrations, sometimes obtained on different nights and therefore at different parallactic angles, only the azimuthally-averaged radial intensity profile can be established with any accuracy. The beam at each wavelength has therefore been fitted with the sum of two circular Gaussians (Table 2), more detailed modeling of the beam not being justified by the data. This produces excellent fits to the beam profiles, and demonstrates that within a radius of 60 arcsec 80% of the total power is in the central diffraction spike at 850 μm , reducing to 40% at 350 μm . The beam was not measured at 1.3 mm, but a 22-arcsec Gaussian (FWHM) has been assumed when comparing the 1.3 mm photometry with data at shorter wavelengths.

4. Results

4.1. Images

Fig. 2 displays the SCUBA images of the eight protostars. The greyscale is linear and spans the whole range of emission, while the contours are logarithmic to emphasize the faint, extended structure. An arrow in the 850 μm image shows the orientation of the blueshifted outflow for each source. A glance at the four protostars in Taurus shows immediately a trend between the spatial distribution of the submillimeter dust emission and the spectral classification of the objects: the Class 0 source, L1527, comprises a central peak along with a considerable extended envelope. The Class I protostars L1551 IRS5 and TMC1A have comparable fractions of emission in an extended component compared with the central peak, in spite of the fact that the luminosity of these two sources differs by a factor of ten. The emission from the Class II source HL Tau is more compact than the other three sources, although there remains some extended emission even around this object.

The images of the protostars in Perseus illustrate well the different mode of star formation taking place in this cloud, which contains many sources a factor of ten more luminous than those in Taurus. The youngest protostar of the sample is probably HH211-mm (see Section 6 below), and like L1527, the dust emission from this object is very extended with the envelope dominating over any compact source. The L1448 field contains not only the Class 0 protostar L1448-mm (also known as L1448C), but also several sources associated with the bright IRAS source IRS3 to the north. IRS3 is now known to comprise a Class 0 binary system, L1448N, which appears as an elongated source at position angle $\sim 45^\circ$ in Fig. 2, along with another Class 0 companion 20 arcsec away from the IRAS position, L1448NW (Terebey & Padgett 1997; Barsony et al. 1998). Approximately 30 arcsec to the southeast of the peak submillimeter emission from NGC1333 IRAS2 a second embedded object is detected at all wavelengths (see also Sandell et

al. 1994). In order to distinguish the main bright peak from this second source we designate them IRAS2:CR1 and IRAS2:CR2 respectively. The ridge of dust emission from SVS13 was first resolved into three protostars by Chini et al. (1997) at 1.3 mm and referred to as MMS1, MMS2, and MMS3. The same sources are now also observed at submillimeter wavelengths in Fig. 2. In the 850 μm image of SVS13 diamonds show the positions of the water masers found by Haschick et al. (1980), and the crosses in the SVS13 images at all wavelengths give the positions of the VLA sources reported by Rodríguez et al. (1997).

4.2. Continuum spectra

Flux densities integrated within a radius of 45 arcsec for all the program sources are listed in Table 3, and are plotted as spectra along with measurements at other wavelengths available from the literature in Fig. 3. It is from the spectra in Fig. 3 that the luminosities listed in Table 1 have been derived. They suggest that the 750 μm fluxes are consistently too low compared with the other submillimeter measurements, by approximately 10–15%. While this is within the 1σ calibration uncertainties the fact that every source is systematically low at 750 μm suggests some other problem with the calibration which we have not been able to identify, in spite of checking these data extremely carefully. Alton, Davies, & Bianchi (1999) also report a similar problem with 750 μm SCUBA data, although to a much greater extent than that found here.

Table 3 and Fig. 3 also give flux densities for other sources detected in our SCUBA images. Flux densities for both L1448N and L1448NW are plotted separately, and the NGC1333 IRAS2 region has been further separated into IRAS2:CR1 and IRAS2:CR2. Submillimeter dust emission from the SVS13 region originates from the ridge containing MMS1, MMS2, and MMS3, and the flux densities listed in Table 3 are derived from CLEANed images as described in Section 6. They are flux densities per 11-arcsec beam, for comparison with the 1.3 mm measurements given by Chini et al. (1997).

The extended emission associated with L1527 is not resolved into a binary companion as reported by Fuller, Ladd, & Hodapp (1996), but instead is a continuous, low-level distribution tracing three arms of a cross. The emission from L1527 has therefore not been separated into multiple components, and Table 3 and Fig. 3 give only integrated flux densities for this source. The HL Tau field also covers the position of the T Tauri star XZ Tau, 23 arcsec to the east. The only wavelength for which there is a statistically significant detection of submillimeter continuum emission at the position of XZ Tau is 850 μm , but almost half of the 70 mJy beam⁻¹ measured in this image is caused by the error beam associated with HL Tau, leaving a 3σ upper limit for the 850 μm flux density of XZ Tau of 48 mJy beam⁻¹. Assuming a spectrum $F_\nu \propto \nu^3$ for any disk component associated with XZ Tau, the 3σ limits obtained from the rms noise in each image

(Table 3) correspond to ~ 10 to 20 mJy beam^{-1} at a wavelength of 1.3 mm , similar to the limit measured by Beckwith et al. (1990).

5. Radial profile analysis

5.1. Description of models

The major advantage of using dust emission for analyzing the structure of protostellar envelopes derives from its simple radiative transfer. At submillimeter wavelengths the emission is optically thin, and the dust opacity is a power-law function of frequency, typically written as $\kappa_{\nu} = \kappa_0(\nu/\nu_0)^{\beta}$, where β lies in the range 0 to 2 depending on the grain size, shape, and composition (e.g., Miyake & Nakagawa 1993; Pollack et al. 1994; Agladze et al. 1994, 1996). Although β is not well known, we will demonstrate that this is not a significant problem for deriving density profiles from the dust emission. The absolute value of the dust opacity is also uncertain to factors of 5 or so, but will primarily result in highly uncertain masses derived from the dust emission, and does not influence the derived density distributions.

The model assumes a spherically symmetric envelope, and the intensity distribution of the dust emission in the SCUBA images is used to derive the radial density profile in the envelope. The density profile is a power law, $\rho \propto r^{-p}$, the value of p derived using this method depending upon the assumed temperature distribution. For a power law temperature profile, $T \propto r^{-q}$, this dependence of p on the form of $T(r)$ is easily demonstrated for the extreme limit of low optical depth, in the Rayleigh-Jeans regime. In this limit, such power-law profiles will result in the intensity distribution of the dust emission, as a function of angular distance on the sky, having the form

$$I_{\nu} \propto \theta^{1-(p+q)}. \quad (1)$$

Values of p derived from $I_{\nu}(\theta)$ will therefore be sensitive to the value of q adopted. The model uses the analytical expression for the temperature distribution,

$$T(r) = 60 \left(\frac{r}{2 \times 10^{15} \text{ m}} \right)^{-q} \left(\frac{L_{\text{bol}}}{10^5 L_{\odot}} \right)^{q/2} \text{ K}, \quad (2)$$

where $q = 2/(4 + \beta)$. This arises from balancing the heating and cooling of a dust grain at radius r from a source of luminosity L_{bol} (Chandler et al. 1998), and is a generalization of the expressions derived by Scoville & Kwan (1976), normalized to match the more detailed radiative transfer calculations of Wolfire & Churchwell (1994). Equation 2 is assumed to hold until the temperature falls to the temperature of the ambient cloud. The value of β is not precisely known, but the 850 to $450 \mu\text{m}$ spectral indices, α (where $F_{\nu} \propto \nu^{\alpha}$), lie between 2.6 and 3.1 for all the sources. Including

a correction for the shape of the Planck curve it is therefore likely that β is in the range 1 to 2, so temperature profiles which follow Equation 2 with $\beta = 1$ ($q = 0.4$) to a minimum ambient temperature of $T_{\text{amb}} = 10$ K, and one with $\beta = 2$ ($q = 0.33$) down to $T_{\text{amb}} = 14$ K, are taken as two extremes of possible temperature distributions.

In view of the uncertainty in the orientation on the sky of the error beam of the telescope, particularly after several integrations have been co-added, only azimuthally-averaged radial intensity profiles are considered in deriving envelope density distributions from the submillimeter dust emission. The radial intensity profile for each source is fitted by a combination of the emission from an envelope, as described above, and a disk, which on the scale of these measurements is a point source. The envelope emission at submillimeter wavelengths is assumed to be optically thin throughout, and the best-fit models verify that this assumption is valid. The Rayleigh-Jeans approximation is *not* assumed to hold, and corrections for the shape of the Planck curve are included in the model. The intensity profiles are fitted by varying the index of the radial density power law, p , and the fraction of the flux originating in the envelope, $f_{\text{env}} = F_{\text{env}} / (F_{\text{env}} + F_{\text{disk}})$, where F_{env} is the envelope flux and F_{disk} is the flux in the central point source (disk). Clearly, the value of F_{env} (and therefore f_{env}) will depend upon the outer radius assumed for the envelope. Emission is present in the images even on the largest scales, with no obvious outer radius for the envelopes evident in the data. Since a chop throw of 120 arcsec is used, the envelopes have been modeled with radial angular extents $\theta_o = 60''$. However, the effect of larger outer radii on the derived value of p has also been investigated by fitting the data with models having $\theta_o = 90''$ as well. The inner radius is fixed at 100 AU, but the results are insensitive to its precise value since these small radii contribute very little to the envelope flux at these wavelengths.

The model intensity profile of the combined disk/envelope system is computed for given values of p and f_{env} , it is convolved with the model beam (Table 2), and a DC offset with the value of the convolved model at $\theta = 60''$ is subtracted to simulate observation with the 120-arcsec chop throw. Since structure remains in the images at position angles perpendicular to the chop direction, the same procedure of subtracting a DC offset from the data was carried out before calculating the radial profiles for comparison with the models.

5.2. Modeling results

Most of the sources exhibit relatively simple structure in their dust emission, and a symmetrical envelope is not an unreasonable model. An obvious exception is the case of SVS13, where the narrow ridge contains three separate protostars and a spherical envelope model is clearly inappropriate. No attempt has therefore been made to model the emission from SVS13. With one exception the images used for the radial profile fitting are those displayed in Fig. 2. For

NGC1333 IRAS2:CR1, however, it was clear that the nearby source IRAS2:CR2, and possibly the extension to the northwest, might affect the profile analysis. These two regions of emission have therefore been selectively blanked before forming the azimuthally-averaged profile.

Both the data and the model are averaged into 3-arcsec bins, and the χ^2 is calculated for a given value of p and f_{env} using the statistical uncertainty at each data point. The value of f_{env} is not necessarily the same at each wavelength, and depends on the relative values of the spectral index of the envelope and disk components as a function of wavelength. To avoid introducing further free parameters into the modeling each source and each wavelength have therefore been fitted separately. A range of p from 0 to 5 is covered, and of f_{env} from 0 to 1. These χ^2 surfaces are then used to evaluate confidence limits for p and f_{env} . Fig. 4 illustrates the results for individual sources by plotting the 850 and 450 μm azimuthally-averaged radial profiles. Data are shown along with the model beam and the best-fit model profiles for the case where $\beta = 1$ ($q = 0.4$), $T_{\text{amb}} = 10$ K, $\theta_o = 60''$. The contours enclose the 68.3, 95.4, and 99.7% confidence limits in the χ^2 -surfaces as a function of p and f_{env} . In general, the fitted value of p is positively correlated with f_{env} . Thus models with a steep density gradient in the envelope, where most of the flux originates in the extended component, may fit just as well as those where the value of p is lower, but where more flux comes from the disk. This result is particularly clear for the Class I source TMC1A, and the Class II object HL Tau, both of which have very centrally-peaked profiles. In these cases the model does not distinguish well between a large value of p and a high f_{env} , and low p , low f_{env} .

For each source the overall shape of the χ^2 surface is similar at all wavelengths, an encouraging sign that the model beams used are reasonable. The absolute value of the χ^2 is probably not very meaningful, since systematic uncertainties in the beam shape have not been included in the calculation of the statistical uncertainties. Nevertheless, relative values are useful for inter-comparison between sources. The strongest constraints on p and f_{env} are obtained from the 850 μm data, where the signal-to-noise ratio is the highest. Since the point spread function at 850 μm is also less likely to be affected by asymmetries introduced by the chop throw and by the error beam (Fig. 1), and the emission is the most optically thin of all the wavelengths modeled, we conclude that the results obtained from fitting the 850 μm profiles are the most reliable. The best 850 μm fits are found for HH211-mm, although good fits are also obtained for TMC1A, L1527, and L1448-mm. The best fits for L1551 IRS5, HL Tau, and NGC1333 IRAS2:CR1 are not formally “good” fits based on the statistical uncertainties.

In order to examine possible evolutionary traits we would ideally like to compare the fitted values of p and f_{env} with a continuously varying function of protostellar age, such as the bolometric temperature, T_{bol} , proposed by Myers & Ladd (1993). Unfortunately no far-infrared measurements are available to constrain the short-wavelength turnover for the spectrum of HH211-mm, so its T_{bol} cannot be calculated. Nevertheless, the spectra in Fig. 3 have been used to

calculate T_{bol} for the other protostars, and assuming HH211-mm to be the youngest, the sources may be ranked according to age within a given spectral class. Fig. 5 summarizes the results of the profile fitting by plotting the best-fit values of p and f_{env} , along with error bars corresponding to 95% confidence limits, as a function of spectral class within which our sources are ranked as described above. Only results for the 850 μm data and $\theta_o = 60''$ are shown, but the temperature profiles corresponding to both $\beta = 1$ and $\beta = 2$ are included.

For many of the sources the best-fit values of p derived from the 850, 750, 450, and 350 μm images tend to decrease with decreasing wavelength. However, because the dynamic range in the 750, 450, and 350 μm images is lower than that at 850 μm , the ranges of p and f_{env} which give acceptable fits to the data are larger. The value assumed for θ_o affects both f_{env} and p . Higher values of f_{env} are obtained for larger θ_o , for obvious reasons. The influence of θ_o on p is slightly more subtle, and arises because of the subtraction of the 60-arcsec DC level. This truncation has the effect of steepening the output intensity profile in the model for $\theta_o = 90''$, and so values of p lower by approximately 0.1 are needed to fit the data compared with $\theta_o = 60''$. From Equation 1 it is clear that the assumption of $\beta = 1$ compared with $\beta = 2$ will give values of p differing by at least 0.1. In fact, the fits to the measured intensity profiles show that p derived assuming $\beta = 1$ are approximately 0.2 lower than those for $\beta = 2$, the extra 0.1 originating from the flattening of the temperature profile at a higher ambient temperature for $\beta = 2$ in our model.

Fig. 5 shows that the 95% confidence limits for p encompass the values 1.5–2 expected for the collapse of non-singular isothermal spheres, for most sources. The large uncertainty in p for TMC1A and HL Tau arises because of the low f_{env} in these sources. However, the decrease in p from values of around 2 in Class 0 objects to 1.5 in Class I and II sources predicted by the non-singular collapse solutions is not observed. Indeed, it is the protostars believed to be the youngest in our sample which appear to have the most shallow density profiles in their envelopes. This result is made all the more extreme when the values of f_{env} obtained from the model are compared with those actually measured. Some of the sources have had F_{disk} determined directly through observations using the interferometric link between the JCMT and CSO (Lay et al. 1994; Brown et al. 1999). Others have interferometry measurements of the disk flux at millimeter wavelengths (Guilloteau et al. 1992; Chandler, Carlstrom, & Terebey 1994; Hogerheijde et al. 1997; Gueth & Guilloteau 1999), which can be extrapolated to 850 μm assuming reasonable extremes of the spectral index of the disk emission at millimeter/submillimeter wavelengths to be 2 and 3 (Beckwith & Sargent 1991). The range of “measured” values for f_{env} calculated using these disk fluxes and the integrated 850 μm flux densities in Table 3, taking calibration uncertainties into account, are plotted in Fig. 5. They agree with the 95% confidence limits derived from the model fitting, but are typically at the low end of the range. The correlation between f_{env} and p (Fig. 4) demonstrates that low f_{env} requires low p to fit the data, suggesting that the values of p for HH211-mm and L1527 may be even lower than 1.5.

The only models which predict values of p less than 1.5 during collapse are for cores which are initially highly centrally condensed, and which evolve in a manner similar to the Shu solution for the SIS. In these models the shallow density profile occurs immediately interior to the collapse expansion wave, and the size scale on which the shallow density profile is observed should be directly related to the age of the source via the sound speed, a . The ages of HH211-mm and L1527 are very uncertain, but estimates may be obtained from the dynamical timescales of their outflows, which are $\lesssim 10^3$ yr and $\sim 10^4$ yr respectively (Gueth & Guilloteau 1999; Hogerheijde et al. 1998). The age of L1527 has also been estimated to be less than 10^4 yr from modeling of its SED in terms of the Shu picture by Kenyon, Calvet, & Hartmann (1993). For sound speeds $a \sim 0.3$ km s $^{-1}$ the radii of the expansion waves for HH211-mm and L1527 are $\lesssim 0.3''$ and $\sim 5''$, both of which lie within the central beam at $850 \mu\text{m}$. The values of p derived for these sources therefore apply to the structure of their respective cloud cores *outside* the expansion wave, in which case a steep initial density distribution is strongly ruled out. It seems that current models of cloud collapse have problems reproducing our results.

Within the 95% confidence limits our model does not show any evolutionary trends in f_{env} , but the best-fit envelope mass needed to reproduce the observed $850 \mu\text{m}$ flux density, M_{env} , does decrease with spectral class. Fig. 6 illustrates this for $\theta_o = 60''$, where the upper value of each range plotted corresponds to $\beta = 2$, and the lower corresponds to $\beta = 1$, assuming $\kappa_v = 0.01(v/10^{12} \text{ Hz})^\beta \text{ m}^2 \text{ kg}^{-1}$ (Hildebrand 1983). The *measured* f_{env} , on the other hand, clearly does decrease with spectral class, and is primarily caused by a decrease in F_{env} rather than an increase in F_{disk} . These results demonstrate that while the orientation of the embedded protostar/disk/outflow system might have some effect on the shape of the SED it does not *dominate* it, in agreement with the recent work of Chen et al. (1995) and Ladd, Fuller, & Deane (1998).

5.3. Influence of model assumptions on p

The models with which our data are compared are spherically symmetric, as is required of collapse from an initial state of hydrostatic equilibrium in the absence of rotation or other forms of support, such as a magnetic field. While these are probably reasonable as first approximations it is clearly essential that the effect of deviations from the assumptions made in the modeling are examined carefully, and the influence of outflows and other asymmetries on the derived values of p assessed.

5.3.1. Variable β

It is possible that the value of β may vary across the envelopes of the protostars, as has been observed for the dense cores in NGC2024 and Orion A (Visser et al. 1998; Goldsmith, Bergin, & Lis 1997; Johnstone & Bally 1999); such a variation would affect the temperature distribution derived assuming Equation 2. In order to determine whether this may be a problem for our analysis the model beams in Table 2 have been deconvolved from the images presented in Fig. 2, which have then been smoothed to have the resolution of a 22-arcsec Gaussian. The spectral index α has then been calculated across the source in the 1.3 mm scan direction, perpendicular to the outflows. Any systematic changes in α must then be due either to temperature (deviation from the Rayleigh-Jeans regime), optical depth, or β . Fig. 7 shows the value of α derived from the 1.3 mm data and each wavelength/source combination separately. For NGC1333 IRAS2 we found that we were chopping onto emission from SVS13 during the 1.3 mm observations, and so this source has not been included. SVS13 itself was not scanned at 1.3 mm because the source was too complicated for the envelope analysis.

Fig. 7 illustrates that for HL Tau, L1527, L1448-mm, and L1551 IRS5 the spectral index is quite flat as a function of distance. There is, however, some evidence for a decrease in α towards the protostar for HH211-mm, where the trend is in a similar sense to that found for NGC2024. This decrease could be either due to high optical depth in the envelope (unlikely, especially at 850 μm and 1.3 mm), or due to a decrease in β ; since the core is known to contain an embedded protostar the decrease is not likely to be caused by lower temperatures at the center. However, the average difference between the value of α away from the protostar compared with the center of the cloud core is only ~ 0.3 , so even if the effect is caused entirely by a change in β as a function of radius, the two values of $\beta = 1$ and $\beta = 2$ assumed for our modeling should cover all possible extremes. The last source for which α appears to be a function of position is TMC1A, where it tends to decrease away from the central source. This is consistent with lower temperatures at these radii because of its low L_{bol} , an effect which is included in our model.

5.3.2. Outflow cavities and anisotropic density distributions

For speed of computation our model is spherically symmetric, which allows considerable areas of p - f_{env} space to be explored when fitting the data, but does not easily enable the inclusion of the effects of an outflow cavity or other anisotropy in the density distribution. Several models have therefore been constructed including conical outflow cavities, which can also be regarded as extreme cases of flattened, anisotropic, density profiles in the envelope. The four distinct combinations of outflow opening angle and inclination identified by Cabrit & Bertout (1986)

have been examined, and are illustrated schematically in Fig. 8. The resulting normalized radial intensity profiles for the envelopes are also plotted. No central point source has been included, which would only serve to decrease the difference between the various cases as f_{env} decreases. Cases 1, 2, and 3, have outflow semi-opening angles of 30° , and case 4 has a semi-opening angle of 60° . Fig. 8 shows that for those cases which have some fraction of the outflow cavity along the line of sight to the central protostar, cases 1 and 4, the normalized radial intensity profile is more shallow than an envelope with no cavity. Outflow cavities which lie away from the line of sight have profiles slightly steeper, although they are extremely close to the profile obtained for an envelope with no cavity. Since none of the protostars in our sample has case 1 or 4 outflows, the effect of not including an outflow cavity in our model will result in fitted density profiles which, if anything, may be slightly too steep.

5.3.3. Shock heating of dust by the outflow

The one effect which might contribute to the low p derived from our models for L1527 and HH211-mm is if the radial temperature distribution, averaged over all solid angles, does not follow Equation 2 because of sources of heating in the envelope other than radiation from the central protostar. Shock heating at the interface between the cloud and the outflow is demonstrated below to be a possible explanation for the low p derived for L1527 (Section 6), but for HH211-mm the evidence for this in our submillimeter images is less convincing (partly due to its larger distance). There is, however, considerable shocked molecular hydrogen emission associated with the HH211 outflow (McCaughrean, Rayner, & Zinnecker 1994), so shock heating of the dust cannot be altogether discounted. Nevertheless, the solid angle subtended by the HH211 outflow, $\sim 2\%$ of the whole envelope, implies that the mass-weighted temperature of the shock-heated dust must be significantly greater than 50 K for it to increase the *mean* temperature by more than 1 K.

Quantification of the influence of shocks on the mean dust temperature profile of HH211-mm will require higher spatial resolution measurements than those presented here, but the magnitude of the effect can be estimated through the following argument. The time for a dust grain to cool from $\gtrsim 1000$ K to a few tens of K through radiation is very short, on the order of a day. The average dust temperature in the outflow will therefore be determined by other processes, and provided the post-shock density is high enough to couple the dust and gas via collisions, the cooling may actually be dominated by molecular line emission. The excitation temperatures measured in high-velocity molecular gas may therefore be good indicators of the dust temperature in the outflow, and in some sources, the bulk of the high-velocity gas exhibits excitation temperatures have been observed to be 10–20 K higher than the surrounding medium (e.g., Umemoto et al. 1992; Chandler et al. 1996). This enhancement is also comparable to the color

temperature of 25 K derived from 60 and 100 μm dust emission for the L1551 IRS5 flow (Clark & Laureijs 1986; Edwards et al. 1986). However, it is insufficient to affect significantly the mean temperature profile in the envelope of HH211-mm.

5.3.4. *Uncertainties in the distance to Perseus*

The effect of an error in the assumed distance to the Perseus sources has also been investigated, as a fairly wide range of values is reported in the literature. We find that the influence of D on the fitted profile is negligible, which can be seen from the following reasoning. From Equation 2 the physical radius at which the dust temperature has some fiducial value T_0 is proportional to $L_{\text{bol}}^{1/2}$, so the corresponding angular radius is proportional to $L_{\text{bol}}^{1/2}/D$. Since the assumed source luminosity is proportional to D^2 , the angular radius corresponding to T_0 is independent of D . The fitted values of p and f_{env} are thus unaffected by D because the outer radius of the envelope is defined in terms of angular distance, there being no obvious edge to the emission in the images. The main difference between models which assume a different value of D is at small radii, where the inner radius of the envelope is fixed at 100 AU rather than at some value of θ . However, the flux from these inner regions originates typically from less than 1 arcsec in angular extent for values of D between 200 and 350 pc, and so contributes little to the central 10–15 arcsec beam.

6. Structure of individual sources

Extended structure related to the local environment of each source, and possibly the interaction of the source with the surrounding cloud, clearly influences the observed submillimeter emission in Fig. 2 at some level. Features particular to each protostar are described in more detail below, and we discuss how they might affect the derived density profiles.

L1527 The extended dust emission from L1527 delineates three arms of a cross. This structure must be due to a combination of increased column density and/or temperature, and coincides with edges of the outflow cavity defined by the CO(3–2) emission (MacLeod et al. 1994; Hogerheijde et al. 1998). To investigate the relative contributions of density and temperature to the observed submillimeter emission our dust maps have been compared with the high-resolution HCO⁺(1–0) interferometric image of Hogerheijde et al. (1998). We find that the arms of the dust emission coincide very closely with cross features in the HCO⁺. This indicates that at least some of the dust features are caused by a column density enhancement along the edges of the outflow, and

perhaps trace a shell of gas and dust swept-up by the driving wind.

The 450 μm image (Fig. 2) has also been smoothed to match the resolution at 850 μm using the model beams in Table 2, and used to produce a map of the dust color temperature, $T_{450/850}$, in regions which have a sufficiently high signal-to-noise ratio. Fig. 9 illustrates the resulting map as a greyscale, overlaid by the interferometric HCO^+ contours. Assuming a value for β of 1.5 and optically-thin emission, the color temperature is between 10 and 40 K throughout the envelope. However, it clearly is not decreasing monotonically with distance away from the central protostar. A peak in the local dust temperature is located along the northeast arm of the $\text{HCO}^+(1-0)$ cross, at the point where there is a corresponding decrease in HCO^+ emission. The opposite effect can be seen at the end of the southeastern arm, where a small HCO^+ peak coincides with a local minimum in $T_{450/850}$. One possible explanation for this anti-correlation between the $\text{HCO}^+(1-0)$ and $T_{450/850}$ is that the partition function of HCO^+ increases with increasing temperature, suppressing the emission in the $J=1-0$ transition relative to surrounding regions of cooler gas. The coincidence of local temperature peaks with the edges of the outflow cavity lead us to propose that they are caused by shocks, a hypothesis which could be tested through observations of infrared H_2 emission.

The excitation temperature derived for the high-velocity CO emission from the L1527 outflow is 45 K, a significant enhancement over the temperature of the bulk of the molecular gas, 25 K (Hogerheijde et al. 1998). By an argument similar to that given for HH211-mm in Section 5.3.3, the large opening angle of the L1527 flow means that shocks might be an important source of heating away from the protostar, flattening the radial temperature profile in the envelope relative to that possible from radiative heating alone. This might, to some extent, explain our low value of p .

L1551 IRS5 The distinct cross-shaped structure in the submillimeter dust emission from L1551 IRS5 first reported by Ladd et al. (1995) is confirmed by our SCUBA images. These authors also suggested that the origin of the cross feature lies in the interaction of the outflow with the surrounding cloud core, and comparison with the morphology of 2 μm reflection nebulosity (e.g., Hodapp et al. 1988; Lucas & Roche 1996) shows that the orientation of structure in the outflow cavity extends to arcsecond scales. Any contribution to the heating of the envelope around IRS5 by its outflow will tend to result in an underestimate of p . To the northeast of IRS5 the dust emission follows a ridge of molecular gas extending towards L1551NE.

TMC1A Structure in the dust envelope surrounding TMC1A corresponds well to the molecular core in interferometer maps of $^{13}\text{CO}(1-0)$ emission (e.g., Brown & Chandler 1999). While a large range of p fits the radial profiles reasonably well, this source is one for which the shape of

the dust SED is best explained by $p \sim 1$ (Chandler et al. 1998). The SED modeling was carried out using flux densities integrated over the relatively small maps which single-element detector systems were able to produce, and so apply to the envelope close to the source. The radial profile modeling is, on the other hand, more dominated by the points at larger radii, which have lower statistical uncertainties compared with those at the central pixel. It is notable that the observed profile is more shallow than the best-fit $850 \mu\text{m}$ profile shown in Fig. 4 at small radii. Furthermore, the measured f_{env} for TMC1A places the most probable value of p towards the lower end of the distribution plotted in Fig. 5. Thus while a precise estimate of p for the envelope around TMC1A cannot be obtained from the radial profile fitting because of the relatively low fraction of the flux originating in the envelope, a combination of measurements now suggests that its radial density profile is quite flat close to the protostar. This is consistent with the SIS collapse models for a protostar $\sim \text{few} \times 10^4$ yr old, but also the kinematics of the $^{13}\text{CO}(1-0)$ emission show that the envelope is in approximate Keplerian rotation (Ohashi et al. 1997; Brown & Chandler 1999), which might provide the support necessary to explain a value of $p < 1.5$ for non-singular initial conditions.

HL Tau A faint envelope is detected even around the Class II protostar HL Tau. Since the model is not a particularly good description of the source we have investigated whether outer radii of $\theta_o = 30''$ fit the radial profiles better than the $60''$ and $90''$ used for the younger sources, but find it does not. The low level structure is consistent with that expected for a remnant circumstellar envelope most of which has already been dispersed by the outflow or accreted onto the central protostar. The north-south extension evident in Fig. 2 can be traced through molecular line emission to within a few arcsec of the source (Cabrit et al. 1996).

HH211-mm Comparison of the submillimeter continuum emission from HH211-mm with the $\text{H}^{13}\text{CO}^+(1-0)$ image of Gueth & Guilloteau (1999) shows good agreement between the dust distribution and the structure of the dense gas. At the high resolution of 350 and $450 \mu\text{m}$ (Fig. 2) an extension along the direction of the redshifted outflow lobe is also observed. The flow in this source is particularly highly collimated and jet-like, but its larger distance and the resulting low linear resolution of the $850 \mu\text{m}$ data preclude a color temperature analysis similar to that carried out for L1527. The dynamical timescale for the molecular jet is less than 10^3 yr (Gueth & Guilloteau 1999), suggesting the protostar is extremely young.

The semi-opening angle of the outflow cavity at the base of the jet, projected onto the sky, is approximately 15° . This provides an upper limit to the true opening angle, and as Fig. 8 and the discussion in Section 5.3.3 illustrate, suggests that the influence of the outflow on the derived value of p is minimal for this source.

L1448-mm The envelope around L1448-mm is the most circularly symmetric of our Perseus objects, so radiative heating by the protostar is expected to dominate the temperature distribution, with shocks having a relatively small effect on the value of p derived for this source. However, some faint, extended structure at $850\ \mu\text{m}$ is observed towards the north, in the direction of the blueshifted outflow lobe. This feature is also detected in the HIRES-processed IRAS data by Barsony et al. (1998), who suggest that the extended far-infrared emission is associated with the collision of the L1448-mm outflow with an outflow from one of the binary companions comprising L1448N. The reader is directed to the paper by Barsony et al. (1998) for a recent, more detailed description of star formation in the L1448 cloud.

NGC1333 IRAS2 The $1.25\ \text{mm}$ dust emission from NGC1333 IRAS2 was found to be elongated towards the southeast in the IRAM 30-m images presented by Lefloch et al. (1998), but was not resolved into the individual sources IRAS2:CR1 and IRAS2:CR2. IRAS2:CR2 was, however, detected as a separate peak at $800\ \mu\text{m}$ by Sandell et al. (1994). The presence of two distinct outflows originating close to IRAS2 led Sandell et al. to propose that the cloud core harbours a binary system, although molecular line data with sufficiently high resolution are not available for us to determine the relationship between IRAS2:CR2 and these outflows. The complicated structure of the cloud, combined with multiple flows, make the interpretation of the extended emission from NGC1333 IRAS2 in terms of cloud/wind interactions too difficult, and must await more detailed observations.

SVS13 The elongated ridge associated with the infrared source SVS13 was mapped with high resolution in $1.1\ \text{mm}$ and $800\ \mu\text{m}$ continuum emission by Sandell et al. (1990), and has subsequently been resolved into three distinct millimeter sources by Chini et al. (1997). These objects, designated MMS1 (SVS13), MMS2 (also known as SVS13B), and MMS3 by Chini et al., have also been identified interferometrically (Grossman et al. 1987; Bachiller et al. 1999). SVS13B drives an energetic molecular jet (Bachiller et al. 1999), and MMS3 is coincident with radio continuum sources (Rodríguez et al. 1997) and a water maser (Haschick et al. 1980). The resolution of our 350 and $450\ \mu\text{m}$ SCUBA images is sufficient to distinguish MMS1, MMS2, and MMS3, along with extended emission outlining the outflow cavity towards the southeast (see also Lefloch et al. 1998). Our 750 and $850\ \mu\text{m}$ images do not, however, resolve these sources, and for a more detailed comparison of their spectral energy distributions and determination of their evolutionary states, higher resolution is needed. We have therefore attempted to deconvolve all our SVS13 images using a CLEAN algorithm and our model beams, and have produced maps with the resolution of an 11-arcsec (FWHM) Gaussian to match the $1.3\ \text{mm}$ measurements of Chini et al. This process was very successful at 750 and $850\ \mu\text{m}$, for which the telescope beam of the JCMT is most symmetric, and the result for $850\ \mu\text{m}$ is illustrated in Fig. 10.

Flux densities per 11-arcsec beam are plotted for MMS1, MMS2, and MMS3, in Fig. 3. The absolute errors are dominated by the calibration uncertainties, but comparison between sources can be made with much higher accuracy than implied by the error bars. It can then be seen that there is a trend for the submillimeter spectral index to decrease from MMS1 to MMS2 to MMS3, consistent with these latter sources having lower luminosities and/or being more deeply embedded. High resolution far-infrared measurements will be needed to constrain the SEDs of these objects further, but it seems likely that MMS2 and MMS3 are Class 0 protostars.

7. Discussion and conclusions

We have obtained the best constraints yet on the density profile in protostellar envelopes on scales of a few 1000 AU, and find that a single radial power law for the density is a good fit to the intensity profile of the dust emission. For most sources the observations are consistent with $1.5 \lesssim p \lesssim 2$, as expected for the collapse of an isothermal sphere in an initial (non-singular) equilibrium configuration. There are, however, some notable exceptions. In particular, the value of p derived for the youngest sources in our sample, the Class 0 protostars HH211-mm and L1527, is considerably lower than would be expected from the models described in Section 1, which predict $p \sim 2$ at early times. The density profile may also be relatively shallow for the Class I source TMC1A, but this may be explained either by the shallow profile expected inside the expansion wave for the collapse of highly centrally condensed cloud cores, or by the fact that the protostar has already accreted most of the low-angular momentum material from its envelope, leaving behind material which is centrifugally supported. For the Class 0 protostars, however, other explanations are needed for low p . While there are obvious problems with our radial profile analysis, such as the fact that we do not include an outflow cavity, and that the outer radius of the envelope may be larger than 60 arcsec, most of these simplifications result in p being overestimated, thus accentuating the shallow density distributions.

In the case of L1527 heating due to the interaction of a wind from the protostar with the surrounding envelope may enhance the temperature over that expected from radiative heating alone, and might account for the exceptionally low value of p derived from our modeling. Indeed, the ubiquity of extended dust emission associated with the flows from the protostars in our current sample indicates that submillimeter dust emission may prove to be extremely useful for investigating jet/cloud interactions in other very deeply-embedded protostellar systems. For HH211-mm, however, the solid angle subtended by the outflow is very small, and not even outflow heating seems to be able to explain the intensity profile of the submillimeter dust emission. We therefore believe the shallow density distribution obtained for HH211-mm to be a robust result. Because HH211-mm is the youngest protostar in our sample, this has important implications for

models of cloud collapse.

At a distance of 350 pc, the envelope of HH211-mm is well fitted at all radii by a single power law, $\rho \propto r^{-1.5}$, out to 0.1 pc. Values of p as high as 2 are strongly excluded. The outer parts of the dense cloud core may as yet retain the distribution it had prior to collapse, and distributions flatter than $\rho \propto r^{-2}$ then imply that the core is supported at some level, perhaps by magnetic fields or turbulence. In a picture of star formation where collapse begins from an unstable equilibrium configuration when all such forms of support are lost, the inner parts should, however, have attained a distribution $\rho \propto r^{-2}$. For example, if the final mass of the star forming at the centre is $\sim 1 M_{\odot}$, all the material within a radius of ~ 20 arcsec will, at some stage, have to end up in the star, and the density distribution within this radius would be expected to reflect the r^{-2} predicted by collapse theory. Furthermore, if the dynamical timescale of the outflow from HH211-mm is a rough indicator of the age of this source, the radius of the infall region in the SIS collapse picture is much less than 1 arcsec, ruling out the possibility that the $r^{-1.5}$ density profile represents an extended region of free fall unless the collapse did *not* originate from an equilibrium configuration. Another possibility is that most of the cloud core remains supported and that the support mechanism is lost from the inside out. In this case the accretion rate must be determined by the rate at which support is lost rather than hydrodynamical properties of the envelope, such as the local sound speed.

Our SCUBA measurements demonstrate that the accuracy with which density profiles can be established is no longer limited by the dynamic range available in the single-dish images, but instead is determined by other more systematic problems, such as uncertainties in the beam shape. Our use of azimuthally-averaged intensity profiles was necessitated by the asymmetries in the JCMT beam, and while more detailed, three-dimensional, radiative transfer modeling might be desirable in the future, it is not yet justified by the data. Even within the current analysis the accuracy of measured values of f_{env} , which are needed to provide the strongest constraints on p , is determined by the absolute calibration uncertainties of data obtained at different telescopes through the highly variable terrestrial atmosphere. For Class I/II sources, where the contribution from a disk may be significant, the main problem is therefore obtaining reliable relative calibrations for single-dish and interferometer measurements. Future instruments such as the Smithsonian Submillimeter Array will be very important in this respect, since its coverage of a wide range of spatial scales will enable f_{env} to be determined directly. From the more general perspective of establishing more detailed evolutionary trends in envelope structure the present work is clearly limited by its small sample, and illustrates the need for much larger surveys of entire star forming regions.

The authors are grateful to Ant Whitworth for useful discussions about self-similar collapse

solutions, and the anonymous referee for comments which have clarified and improved the paper. The JCMT is operated by the Joint Astronomy Centre on behalf of the Particle Physics and Astronomy Research Council of the United Kingdom (PPARC), the Netherlands Organisation for Scientific Research, and the National Research Council of Canada. CJC and JSR acknowledge the support of a PPARC Advanced Fellowship and a Royal Society Fellowship respectively.

REFERENCES

- Adams, F. C., Emerson, J. P., & Fuller, G. A. 1990, *ApJ*, 357, 606
- Agladze, N. I., Sievers, A. J., Jones, S. A., Burlitch, J. M., & Beckwith, S. V. W. 1994, *Nature*, 372, 243
- Agladze, N. I., Sievers, A. J., Jones, S. A., Burlitch, J. M., & Beckwith, S. V. W. 1996, *ApJ*, 462, 1026
- Alton, P. B., Davies, J. I., & Bianchi, S. 1999, *A&A*, 343, 51
- André, P., Ward-Thompson, D., & Barsony, M. 1993, *ApJ*, 406, 122
- André, P., Ward-Thompson, D., Motte, F., 1996, *A&A*, 314, 625
- Bachiller, R., Guilloteau, S., Gueth, F., Tafalla, M., Dutrey, A., Codella, C., & Castets, A. 1999, *A&A*, in press
- Barsony, M. 1994, in *ASP Conf. Ser. 65, Clouds, Cores, and Low Mass Stars*, ed. D. P. Clemens & R. Barvainis (San Francisco: ASP), 197
- Barsony, M., Ward-Thompson, D., André, P., & O’Linger, J. 1998, *ApJ*, 509, 733
- Beckwith, S. V. W., & Sargent, A. I. 1991, *ApJ*, 381, 250
- Beckwith, S. V. W., Sargent, A. I., Chini, R. S., & Güsten, R. 1990, *AJ*, 99, 924
- Beichman, C. & Harris, S. 1981, *ApJ*, 245, 589
- Blake, G. A., van Dishoeck, E. F., & Sargent, A. I. 1992, *ApJ*, 391, L99
- Brown, D. W., & Chandler, C. J. 1999, *MNRAS*, 303, 855
- Brown, D. W., et al. 1999, in preparation
- Cabrit, S., & Bertout, C. 1986, *ApJ*, 307, 313
- Cabrit, S., Guilloteau, S., André, P., Bertout, C., Montmerle, T., & Schuster, K. 1996, *A&A*, 305, 527
- Cernis, K. 1990, *Ap&SS*, 166, 315
- Chandler, C. J. 1998, in *ASP Conf. Ser. 148, Origins*, ed. C. E. Woodward, J. M. Shull, & H. A. Thronson (San Francisco: ASP), 237
- Chandler, C. J., Barsony, M., & Moore, T. J. T. 1998, *MNRAS*, 299, 789
- Chandler, C. J., Carlstrom, J. E., & Terebey, S. 1994, in *ASP Conf. Ser. 65, Clouds, Cores, and Low Mass Stars*, ed. D. P. Clemens & R. Barvainis (San Francisco: ASP), 241
- Chandler, C. J., & Sargent, A. I. 1993, *ApJ*, 414, L29
- Chandler, C. J., Terebey, S., Barsony, M., Moore, T. J. T., Gautier, T. N. 1996, *ApJ*, 471, 308

- Chen, H., Myers, P. C., Ladd, E. F., & Wood, D. O. S. 1995, *ApJ*, 445, 377
- Chini, R., Reipurth, B., Sievers, A., Ward-Thompson, D., Haslam, C. G. T., Kreysa, E., & Lemke, R. 1997, *A&A*, 325, 542
- Clark, F. O., & Laureijs, R. J. 1986, *A&A*, 154, L26
- Cohen, M., Harvey, P. M., Schwartz, R. D., & Wilking, B. A. 1984, *ApJ*, 278, 671
- Cohen, M., & Schwartz, R. D. 1983, *ApJ*, 265, 877
- Davidson, J. A., & Jaffe, D. T. 1984, *ApJ*, 277, L13
- Edwards, S., Strom, S. E., Snell, R. L., Jarret, T. H., Beichman, C. A., & Strom, K. M. 1986, *ApJ*, 307, L65
- Elias, J. H., 1978, *ApJ*, 224, 857
- Foster, P. N., Chevalier, R. A., 1993, *ApJ*, 416, 303
- Fuller, G. A., Ladd, E. F., & Hodapp, K.-W. 1996, *ApJ*, 463, L97
- Goldsmith, P. F., Bergin, E. A., & Lis, D. C. 1997, *ApJ*, 491, 615
- Grossman, E. N., Masson, C. R., Sargent, A. I., Scoville, N. Z., Scott, S., & Woody, D. P. 1987, *ApJ*, 320, 356
- Gueth, F., & Guilloteau, S. 1999, *A&A*, 343, 571
- Guilloteau, S., Bachiller, R., Fuente, A., & Lucas, R. 1992, *A&A*, 265, L49
- Haschick, A. D., Moran, J. M., Rodriguez, L. F., Burke, B. F., Greenfield, P., & Garcia-Barreto, J. A. 1980, *ApJ*, 237, 26
- Herbig, G. H., & Jones, B. F. 1983, *AJ*, 88, 1040
- Hildebrand, R. H. 1983, *QJRAS*, 24, 267
- Hodapp, K.-W., Capps, R. W., Strom, S. E., Salas, L., & Grasdalen, G. L. 1988, *ApJ*, 335, 814
- Hogerheijde, M. R., van Dishoeck, E. F., Blake, G. A., & van Langevelde, H. J. 1997, *ApJ*, 489, 293
- Hogerheijde, M. R., van Dishoeck, E. F., Blake, G. A., & van Langevelde, H. J. 1998, *ApJ*, 502, 315
- Holland, W. S., et al. 1999, *MNRAS*, 303, 659
- Hunter, C. 1977, *ApJ*, 218, 834
- Jennings, R. E., Cameron, D. H. M., Cudlip, W., & Hirst, C. J. 1987, *MNRAS*, 226, 471
- Johnstone, D., & Bally, J. 1999, *ApJ*, 510, L49
- Keene, J., & Masson, C. R. 1990, *ApJ*, 355, 635

- Kenyon, S. J., Calvet, N., & Hartmann, L. 1993, *ApJ*, 414, 676
- Kenyon, S. J., Dobrzycka, D., Hartmann, L., 1994, *AJ*, 108, 1872
- Ladd, E. F., Fuller, G. A., & Deane, J. R. 1998, *ApJ*, 495, 871
- Ladd, E. F., Fuller, G. A., Padman, R., Myers, P. C., & Adams, F. C. 1995, *ApJ*, 439, 771
- Ladd, E. F., Lada, E. A., & Myers, P. C. 1993, *ApJ*, 410, 168
- Ladd, E. F., Myers, P. C., & Goodman, A. A. 1994, in *ASP Conf. Ser. 65, Clouds, Cores, and Low Mass Stars*, ed. D. P. Clemens & R. Barvainis (San Francisco: ASP), 19
- Larson, R. B. 1969, *MNRAS*, 145, 271
- Lay, O. P., Carlstrom, J. E., Hills, R. E., & Phillips, T. G. 1994, *ApJ*, 434, L75
- Lefloch, B., Castets, A., Cernicharo, J., Langer, W. D., & Zylka, R. 1998, *A&A*, 334, 269
- Lucas, P. W., & Roche, P. F. 1996, *MNRAS*, 280, 1219
- MacLeod, J., Avery, L., Harris, A., Tacconi, L., & Schuster, K. 1994, *JCMT Newsletter No. 3*, 46
- McCaughrean, M. J., Rayner, J. T., & Zinnecker, H. 1994, *ApJ*, 436, L189
- Miyake, K., & Nakagawa, Y. 1993, *Icarus*, 106, 20
- Mundy, L. G., et al. 1996, *ApJ*, 464, L169
- Myers, P. C., & Ladd, E. F. 1993, *ApJ*, 413, L47
- Ohashi, N., Hayashi, M., Ho, P. T. P., Momose, M., Tamura, M., Hirano, N., & Sargent, A. I. 1997, *ApJ*, 488, 317
- Penston, M. V. 1969, *MNRAS*, 144, 425
- Pollack, J. B., Hollenbach, D., Beckwith, S., Simonelli, D. P., Roush, T., & Fong, W. 1994, *ApJ*, 421, 615
- Rodríguez, L. F., Anglada, G., & Curiel, S. 1997, *ApJ*, 480, L125
- Sandell, G. 1994, *MNRAS*, 271, 75
- Sandell, G. 1998, *Secondary Calibrators for SCUBA*,
<http://www.jach.hawaii.edu/JCMT/scuba/astronomy/calibration/calibrators.html>
- Sandell, G., Aspin, C., Duncan, W. D., Robson, E. I., & Dent, W. R. F. 1990, *A&A*, 232, 347
- Sandell, G., Knee, L. B. G., Aspin, C., Robson, I. E., & Russell, A. P. G. 1994, *A&A*, 285, L1
- Sargent, A. I., & Beckwith, S. V. W. 1991, *ApJ*, 382, L31
- Scoville, N. Z., Kwan, J., 1976, *ApJ*, 206, 718
- Shu, F. H., 1977, *ApJ*, 214, 488

- Strom, K. M., Strom, S. E., Edwards, S., Cabrit, S., & Skrutskie, M. F. 1989, *AJ*, 97, 1451
- Terebey, S., & Padgett, D. L. 1997, in *IAU Symp. 182, Herbig-Haro Flows and the Birth of Low Mass Stars*, ed. B. Reipurth & C. Bertout (Dordrecht: Kluwer), 507
- Terebey, S., Shu, F. H., & Cassen, P. C. 1984, *ApJ*, 286, 529
- Umamoto, T., Iwata, T., Fukui, Y., Mikami, H., Yamamoto, S., Kameya, O., & Hirano, N. 1992, *ApJ*, 392, L83
- Visser, A. E., Richer, J. S., Chandler, C. J., & Padman, R. 1998, *MNRAS*, 301, 585
- Walker, C. K., Adams, F. C., & Lada, C. J. 1990, *ApJ*, 349, 515
- Ward-Thompson, D., Scott, P. F., Hills, R. E., André, P., 1994, *MNRAS*, 268, 276
- Weintraub, D. A., Sandell, G., & Duncan, W. D. 1989, *ApJ*, 340, L69
- Whitworth, A., & Summers, D. 1985, *MNRAS*, 214, 1
- Wolfire, M. G., Churchwell, E., 1994, *ApJ*, 427, 889

Fig. 1.— Linear greyscale images of Mars obtained in 1998 January, at wavelengths of 850, 750, 450, and 350 μm . Contours are logarithmic, and are drawn at 2, 4, 8, 16, 32, and 64% of the peak in each case. The direction of the 120-arcsec chop throw is marked in the 850 μm image. The beam is clearly extended in the chop direction even at 850 μm , and at 450 and 350 μm the beam comprises a central diffraction spike, and an approximately triangular error pattern which becomes more symmetric on large scales.

Fig. 2.— Submillimeter continuum images of the eight protostars observed with SCUBA, at 850, 750, 450, and 350 μm . The greyscale is linear and spans the full range of emission. The contours are logarithmic starting at a level of 2σ and spaced by intervals of $\times 1.73$. The rms noise for all the sources at all wavelengths is listed in Table 3. An arrow in the 850 μm image, of length 60 arcsec for reference, shows the direction of the blueshifted outflow for each source. All images cover $220 \times 220 \text{ arcsec}^2$. The positions of the H_2O masers reported by Haschick et al. (1980) are plotted as diamonds in the 850 μm image of SVS13, and the VLA sources from Rodríguez et al. (1997) are shown as crosses. The dotted contours outline the edges of the areas covered by SCUBA.

Fig. 3.— Continuum spectra for the eight protostars in our sample. For panels containing spectra for just one source, the SCUBA flux densities, integrated within a radius of 45 arcsec, are shown as filled triangles. Other measurements obtained in large beams are open squares. For the L1448 field flux densities for the protostellar binary L1448N, and the Class 0 protostar L1448NW, are also plotted, derived as described in the notes to Table 3. In this case, and in other panels containing spectra for multiple sources, separate symbols have not been used for the SCUBA points, to avoid the plots becoming too confused. The integrated flux density from NGC1333 IRAS2 within a 45-arcsec radius is given along with the separate measurements for the central protostar IRAS2:CR1, and the southeastern source IRAS2:CR1 (Table 3). Emission from the three protostars in the SVS13 ridge has been separated by deconvolving the images as described in the text, and are in units of Jy per 11-arcsec Gaussian beam. References for non-SCUBA flux densities are as follows. L1527: far-infrared measurements have been obtained from HIRES-processed IRAS images (unpublished). L1551 IRS5: near/mid-infrared data are from Cohen & Schwarz (1983) and Beichman & Harris (1981); far-infrared data are from Davidson & Jaffe (1984) and Cohen et al. (1984); millimeter/submillimeter data are from Ladd et al. (1995) and Walker, Adams, & Lada (1990); the 3.4 mm measurement comes from Keene & Masson (1990). TMC1A: references are given by Chandler et al. (1998). HL Tau: infrared measurements are from Strom et al. (1989); millimeter/submillimeter data come from Weintraub, Sandell, & Duncan (1989), Adams, Emerson, & Fuller (1990), Beckwith & Sargent (1991), Beckwith et al. (1990), Sargent & Beckwith (1991), Mundy et al. (1996), and Blake, van Dishoeck, & Sargent (1992). L1448: all non-SCUBA measurements come from Barsony et al. (1998). NGC1333 IRAS2: far-infrared data are from Jennings et al. (1987); millimeter measurements come from Sandell et al. (1994) and Lefloch et

al. (1998). SVS13: far-infrared data are from Jennings et al. (1987); 1.3 mm flux densities per 11-arcsec beam for MMS1, MMS2, and MMS3 are from Chini et al. (1997). Where multiple measurements are reported for a particular wavelength a weighted mean has been plotted.

Fig. 4.— *Left*: Normalized, azimuthally-averaged, radial profiles for our protostars at 850 and 450 μm (points). The best-fit model for $\theta_o = 60''$ and $\beta = 1$ ($q = 0.4$) is also plotted as a solid line, and the model beam profile from Table 2 is given as a dot-dash line. For NGC1333 IRAS2:CR1 the radial profile is derived from an image blanked as described in the text. *Right*: contours of the 68.3, 95.4, and 99.7% confidence limits as a function of p and f_{env} , with the best-fit values marked by a filled triangle.

Fig. 5.— Best-fit values for p and f_{env} plotted along with 95% confidence limits, as a function of spectral class. The results are derived from the 850 μm profiles and are shown for models with $\theta_o = 60''$. Temperature profiles which assume $\beta = 1$ ($q = 0.4$) are open circles, those with $\beta = 2$ ($q = 0.33$) are filled circles. The range of values for f_{env} obtained directly from measurements are indicated by grey bars. The values of p corresponding to the r^{-2} of a singular isothermal sphere and the $r^{-3/2}$ for free-fall collapse are also marked.

Fig. 6.— Best-fit envelope masses, M_{env} , needed to account for the observed 850 μm flux density, as a function of spectral class. The lower value corresponds to $\beta = 1$, the upper to $\beta = 2$.

Fig. 7.— Spectral indices, α , defined by $F_\nu \propto \nu^\alpha$, between $\lambda = 1.3$ mm and the wavelengths of the other SCUBA filters. The values of α are plotted as a function of position away from the central protostar, along the 1.3 mm scan direction, perpendicular to the outflow from each source.

Fig. 8.— Normalized radial profiles for envelopes having conical outflow cavities, with opening angle and inclination combinations as defined by Cabrit & Bertout (1986). The envelope is the hatched area in all cases. These examples are for $\theta_o = 60''$, and $f_{\text{env}} = 1$. The semi-opening angle of the cavity is 30° for cases 1, 2, and 3, and for case 4 it is 60° . The inclination angles of the outflow symmetry axis to the line of sight are 0° , 45° , 90° , and 45° for cases 1, 2, 3, and 4 respectively, as shown.

Fig. 9.— Greyscale of the 450 to 850 μm dust color temperature for L1527, assuming optically-thin emission and $\beta = 1.5$. The position of the protostar is indicated by a star. Contours of the $\text{HCO}^+(1-0)$ emission from Hogerheijde et al. (1998) are overlaid, illustrating the anti-correlation between local enhancements in the dust temperature and molecular emission, particularly along the eastern arms of the cross.

Fig. 10.— Image of the 850 μm emission from SVS13, after CLEANing with the model beam and reconstruction with an 11-arcsec Gaussian. The positions of the millimeter continuum sources

measured using the Plateau de Bure interferometer by Bachiller et al. (1999) are plotted as asterisks, and are labeled with the names given to these objects by Chini et al. (1997).

Table 1. Source sample.

Source	Cloud	R.A. (2000) (h m s)	Dec. (2000) ($^{\circ}$ ' ")	Ref. ^a	Class	$L (L_{\odot})$
L1448-mm	Perseus	03 25 38.84	30 44 05.4	1	0	14
NGC1333 IRAS2	Perseus	03 28 55.59	31 14 37.5	2	0	35
SVS13	Perseus	03 29 03.75	31 16 03.7	3	II	50
HH211-mm	Perseus	03 43 56.73	32 00 51.9	2	0	$\sim 15^b$
L1551 IRS5	Taurus	04 31 34.15	18 08 05.2	4	I	21
HL Tau	Taurus	04 31 38.41	18 13 57.8	5	II	7
TMC1A	Taurus	04 39 35.16	25 41 45.1	6	I	2
L1527	Taurus	04 39 53.88	26 03 10.2	7	0	2

^aReferences for the positions are as follows: (1) Guilloteau et al. (1992); (2) this paper (for NGC1333 IRAS2 the position is that of the submillimeter continuum peak, designated IRAS2:CR1 in Section 4.1); (3) Bachiller et al. (1999); (4) Keene & Masson (1990); (5) Mundy et al. (1996); (6) Brown & Chandler (1999); (7) Chandler et al. (1994). Positions measured from the SCUBA images are accurate to approximately 3 arcsec.

^bSince only millimeter/submillimeter fluxes are available for HH211-mm, its luminosity has been estimated by comparing its spectrum with those of L1448-mm and NGC1333 IRAS2.

Table 2. Two-component Gaussian fits to the JCMT beam.

λ (μm)	θ_1^a (arcsec)	P_1	θ_2 (arcsec)	P_2
850	13.8	0.78	47	0.22
750	12.4	0.72	43	0.28
450	8.3	0.53	37	0.47
350	7.9	0.41	31	0.59

^aFWHM (θ) and fractional power (P) for Gaussian components 1 and 2, given the Gaussian interpolation from Nasmyth to equatorial coordinates.

Table 3. Integrated submillimeter flux densities for the protostars listed in Table 1.

Source	$\lambda = 850 \mu\text{m}$		750 μm		450 μm		350 μm	
	$F_{\text{int}}^{\text{a}}$ (Jy)	Rms ^b	F_{int}	Rms	F_{int}	Rms	F_{int}	Rms
L1448-mm	5.34±0.43	19	6.91±0.91	30	34.2±6.9	98	58±18	490
L1448N	6.53±0.52	...	8.3±1.1	...	43±12	...	72±22	...
L1448NW	1.84±0.15	...	2.60±0.34	...	13.1±2.6	...	19.5±5.9	...
NGC1333 IRAS2	8.97±0.73	24	11.9±1.6	37	68±14	140	119±36	530
IRAS2:CR1	4.79±0.39	...	6.61±0.86	...	43±11	...	74±22	...
IRAS2:CR2	1.19±0.10	...	1.53±0.21	...	7.7±1.6	...	13.4±4.3	...
SVS13	14.9±1.2	36	21.5±2.8	61	119±24	200	203±61	850
MMS1	2.68±0.22	...	3.82±0.50	...	24.7±7.1	...	40±12	...
MMS2	2.55±0.21	...	3.42±0.45	...	20.1±5.7	...	29.4±8.9	...
MMS3	1.08±0.10	...	1.74±0.23	...	9.2±2.4	...	13.3±4.1	...
HH211-mm	5.73±0.47	21	8.2±1.1	33	34.7±7.0	110	51±16	390
L1551 IRS5	12.1±1.0	22	18.2±2.4	37	94±19	350	164±49	630
HL Tau	2.97±0.25	16	4.04±0.54	20	16.8±4.8	150	26.4±8.7	400
TMC1A	1.80±0.15	8	2.17±0.30	17	12.7±2.6	92	20.6±6.6	300
L1527	5.90±0.48	15	8.4±1.1	21	44.8±9.0	130	66±20	340

^aFor most sources the flux density is integrated over an area 45 arcsec in radius, centered on the central protostar. For L1448-mm a radius of 40 arcsec is used to avoid including emission from L1448N to the north. For L1448N we used 18 arcsec, and for L1448NW the flux is the peak flux per beam obtained from images smoothed to the resolution of the 850 μm data using the model beams listed in Table 2. For NGC1333 IRAS2 we also quote integrated flux densities for IRAS2:CR1 and IRAS2:CR2 separately, using radii of 20 arcsec and 16.5 arcsec respectively. See sections 3 and 6 for a description of the sources MMS1, MMS2, and MMS3.

^b1 σ rms noise for the images shown in Fig. 2, in mJy beam⁻¹.

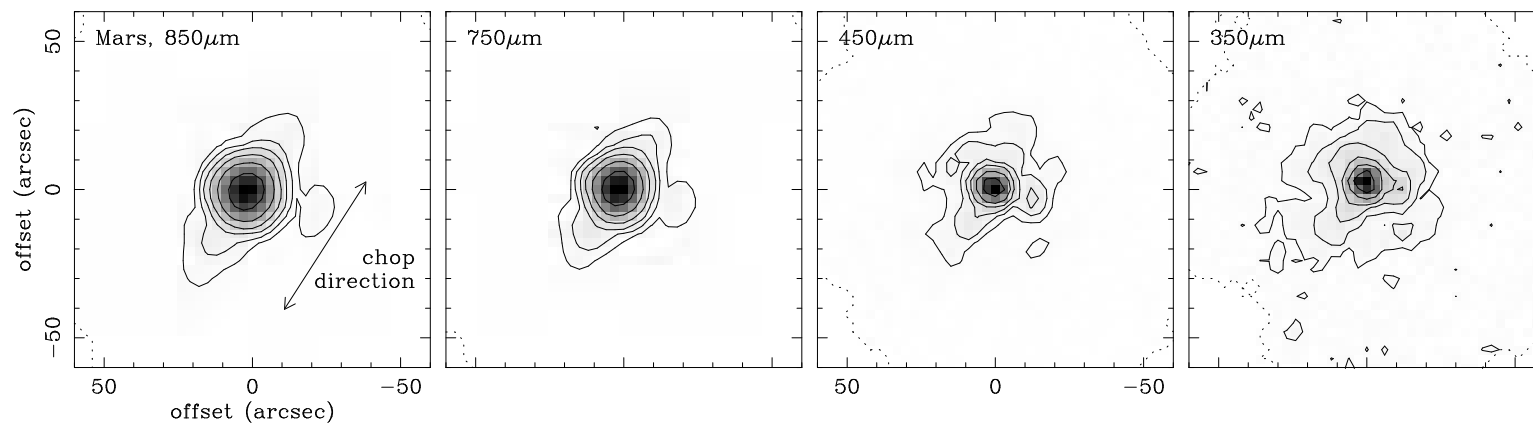


Fig. 1.

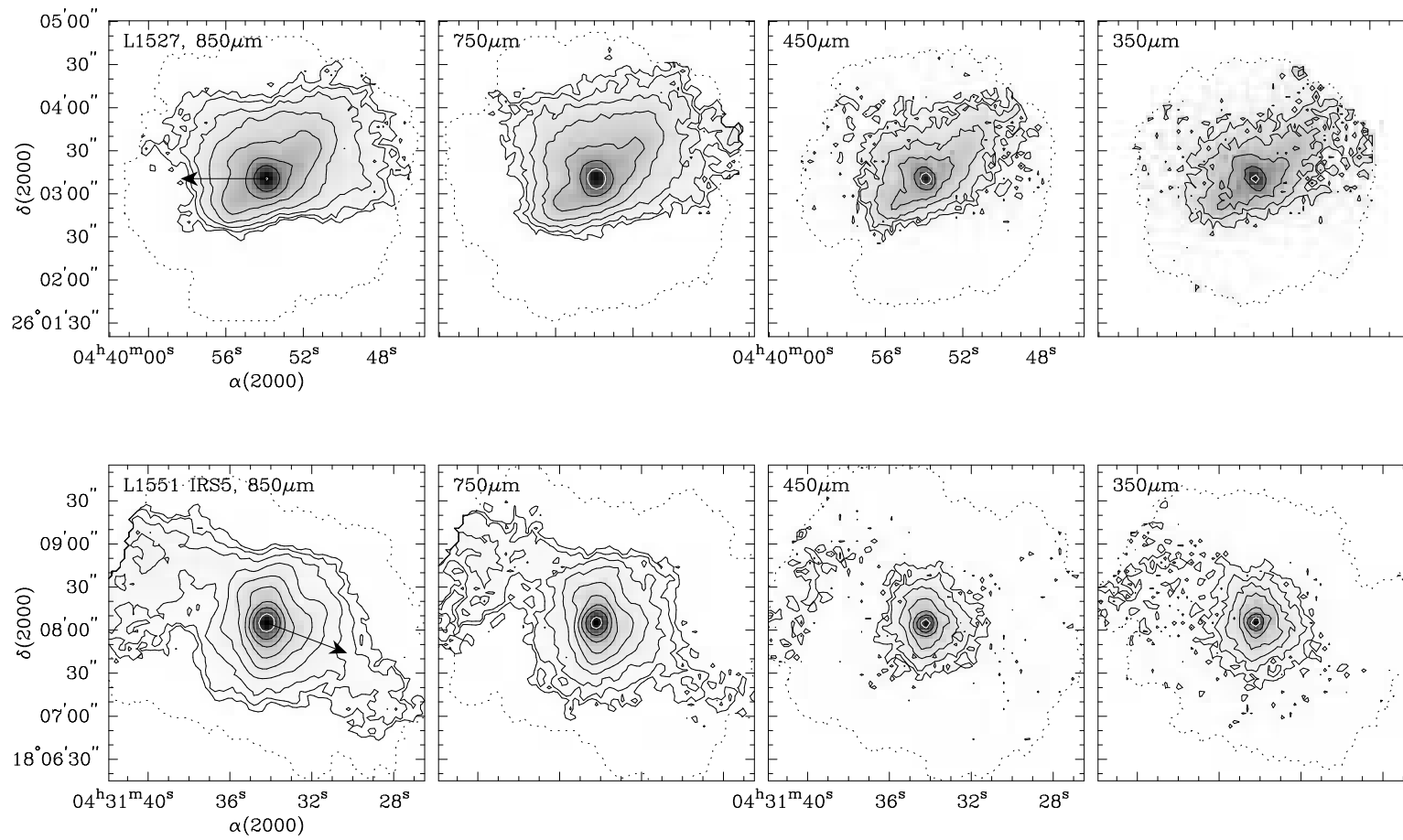


Fig. 2.

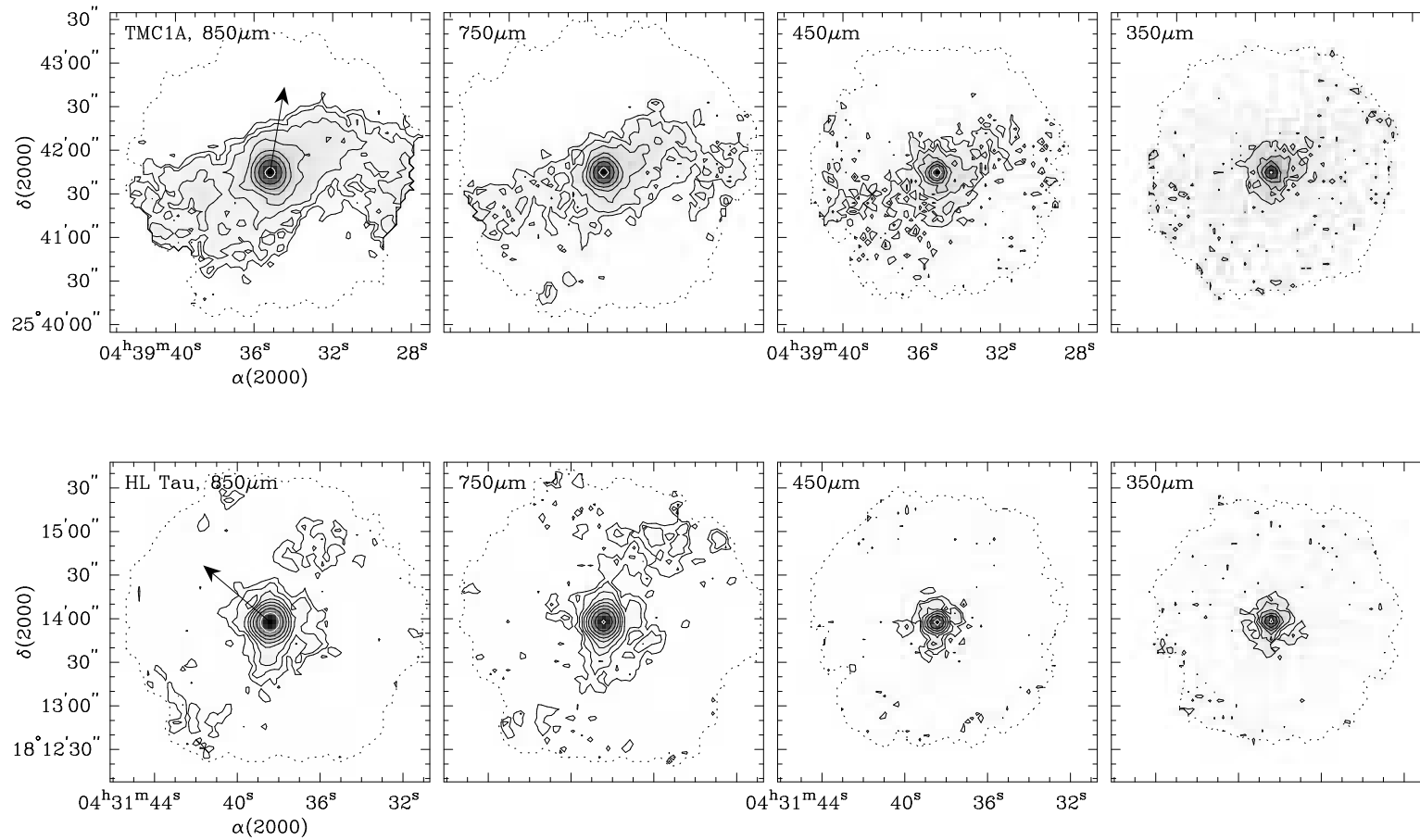


Fig. 2 (cont).

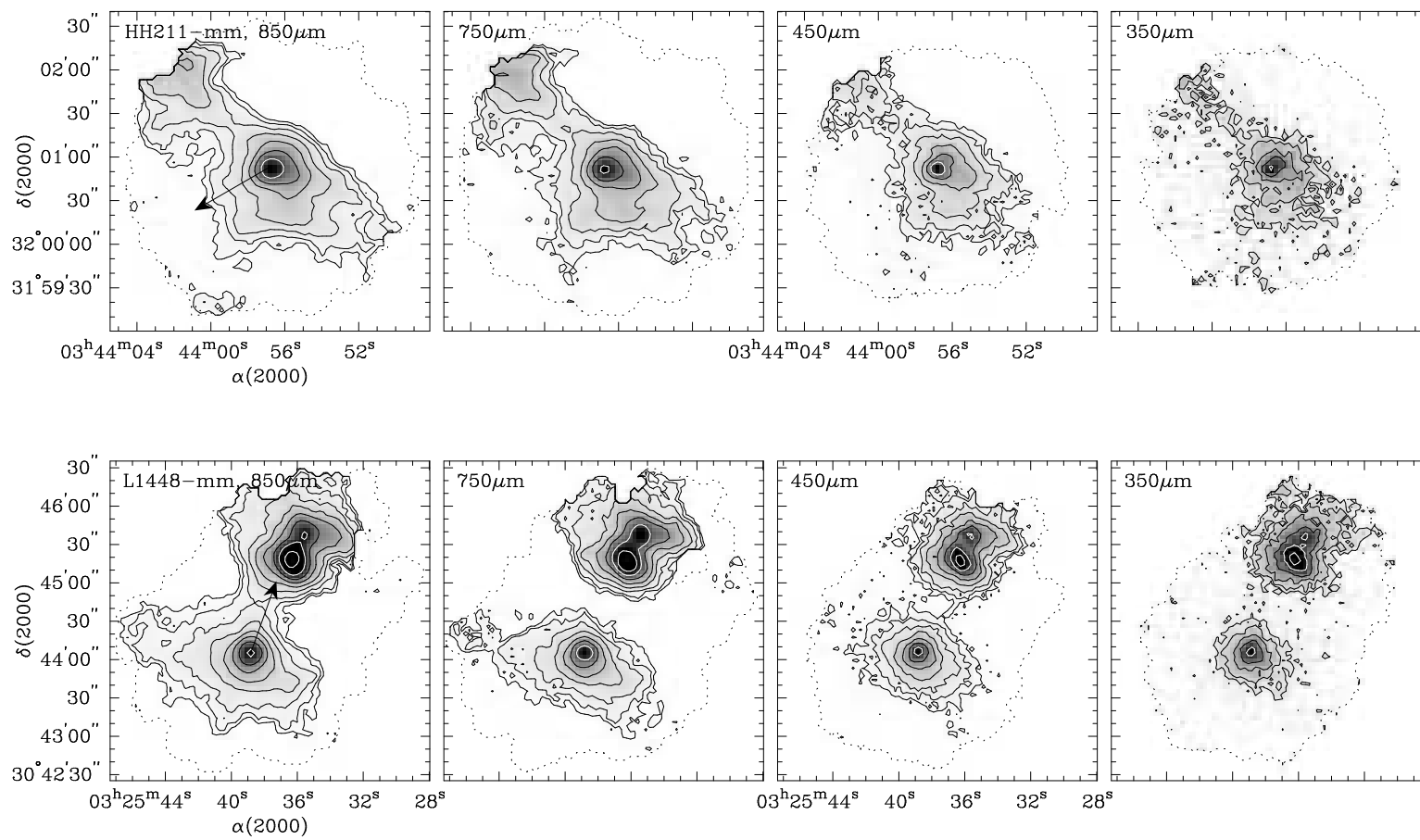


Fig. 2 (cont).

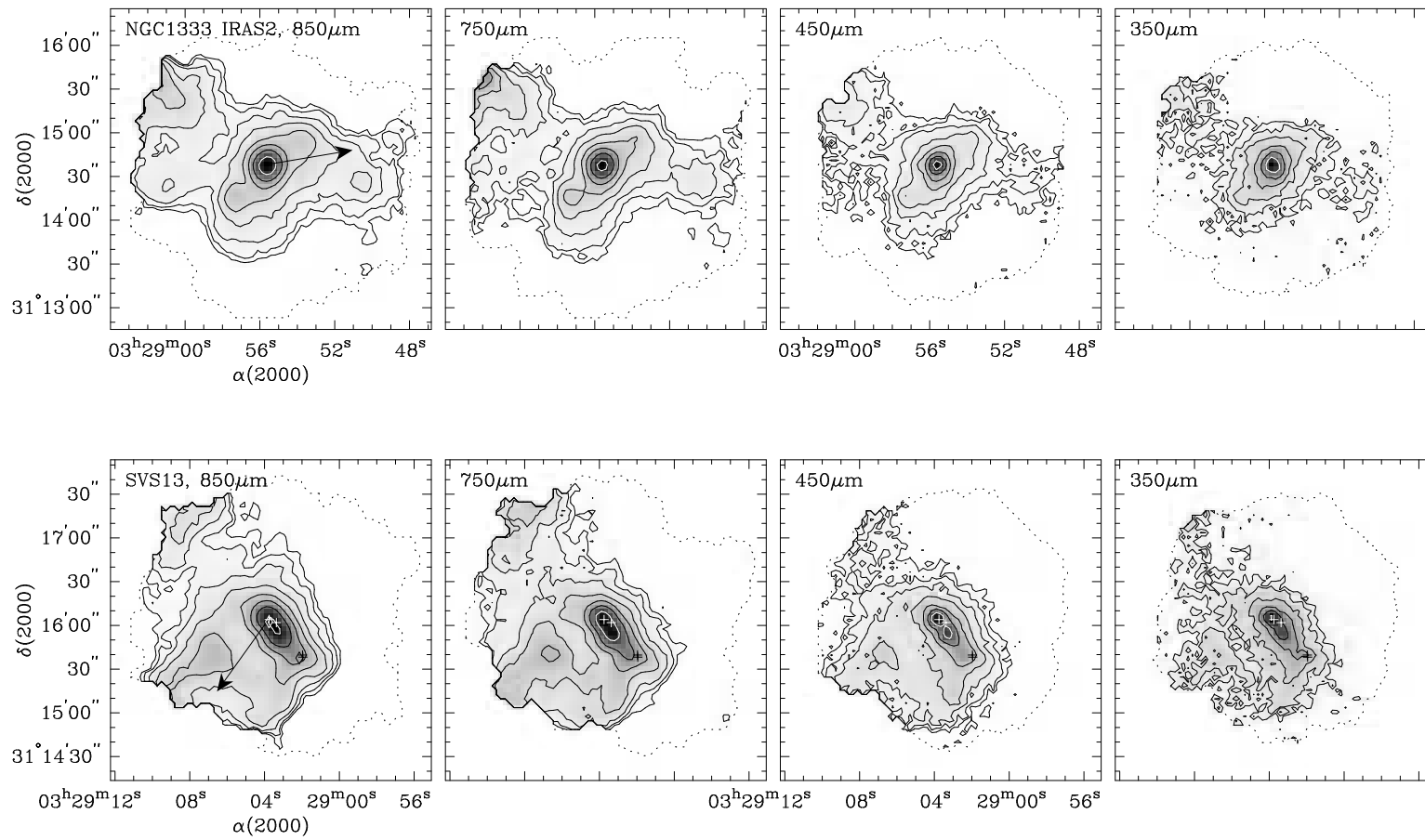


Fig. 2 (cont).

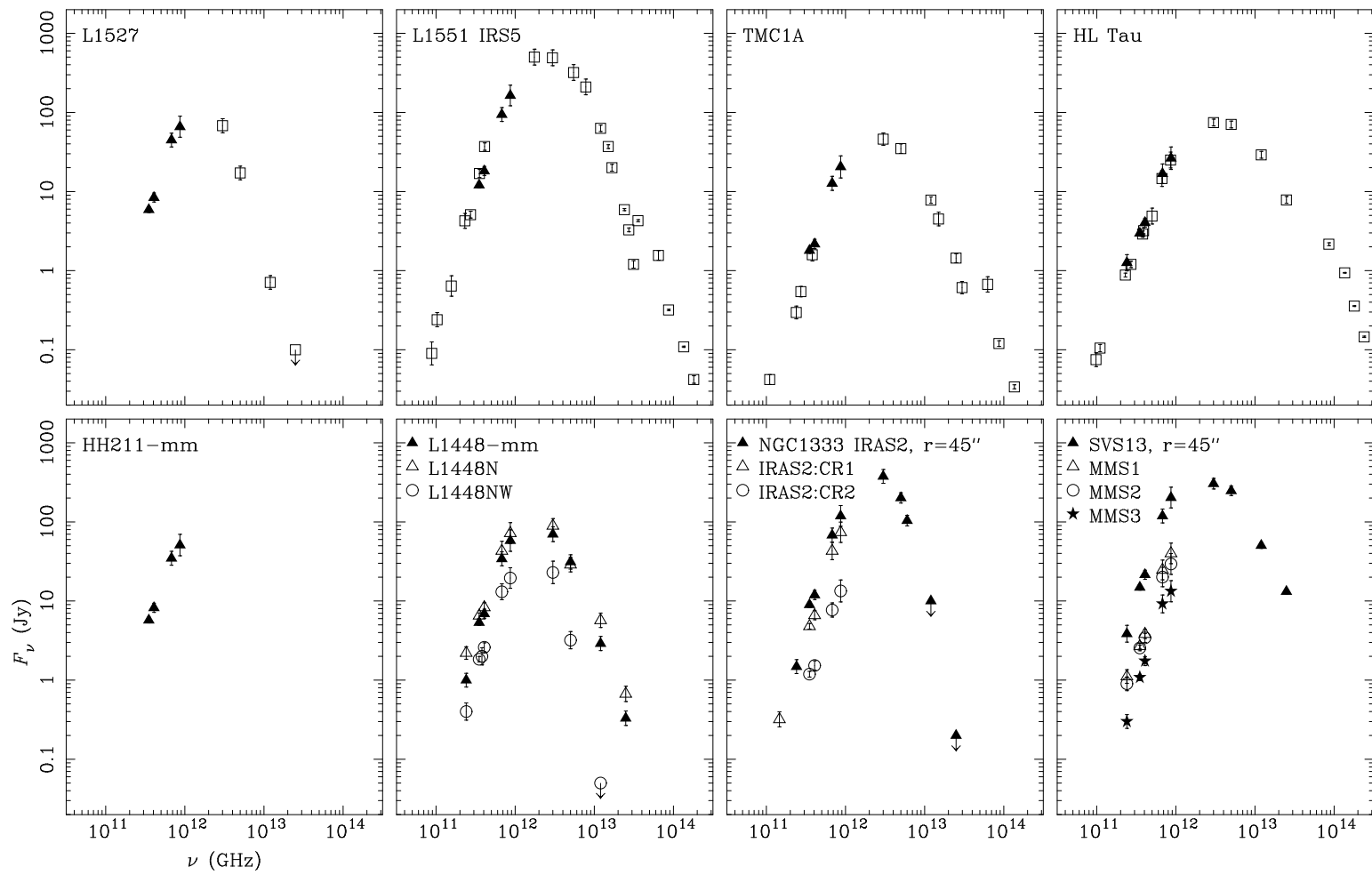


Fig. 3.

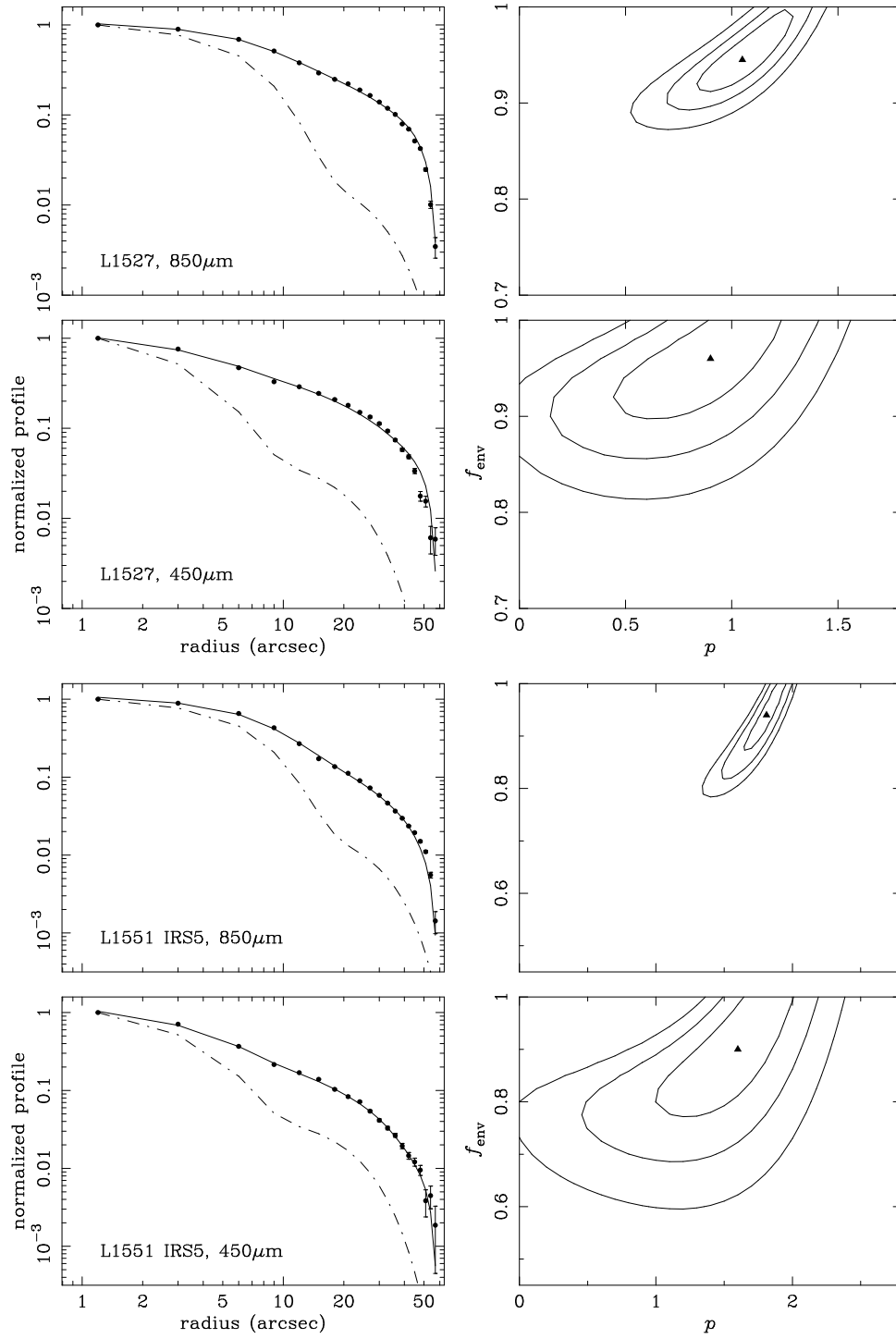


Fig. 4.

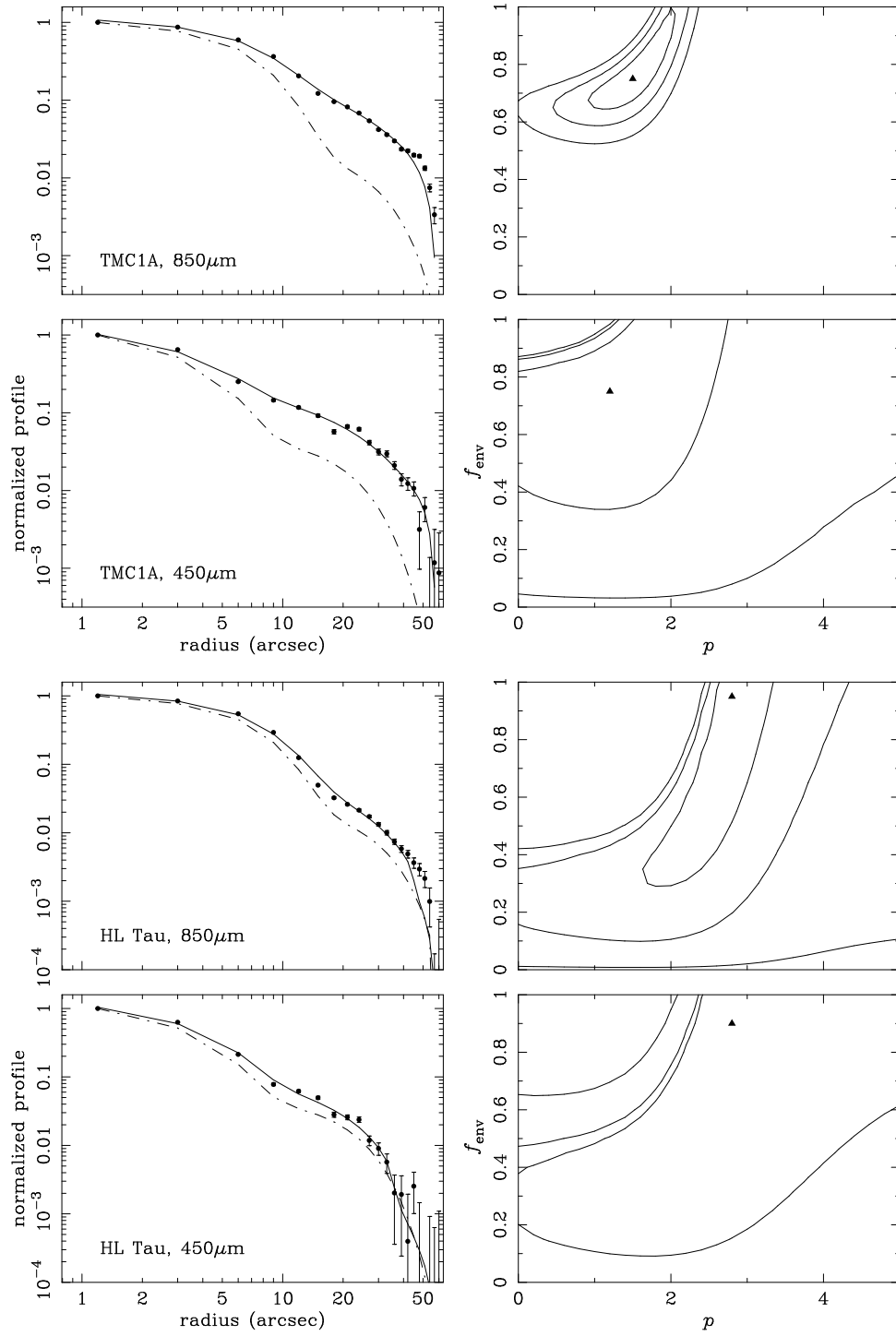


Fig. 4 (cont).

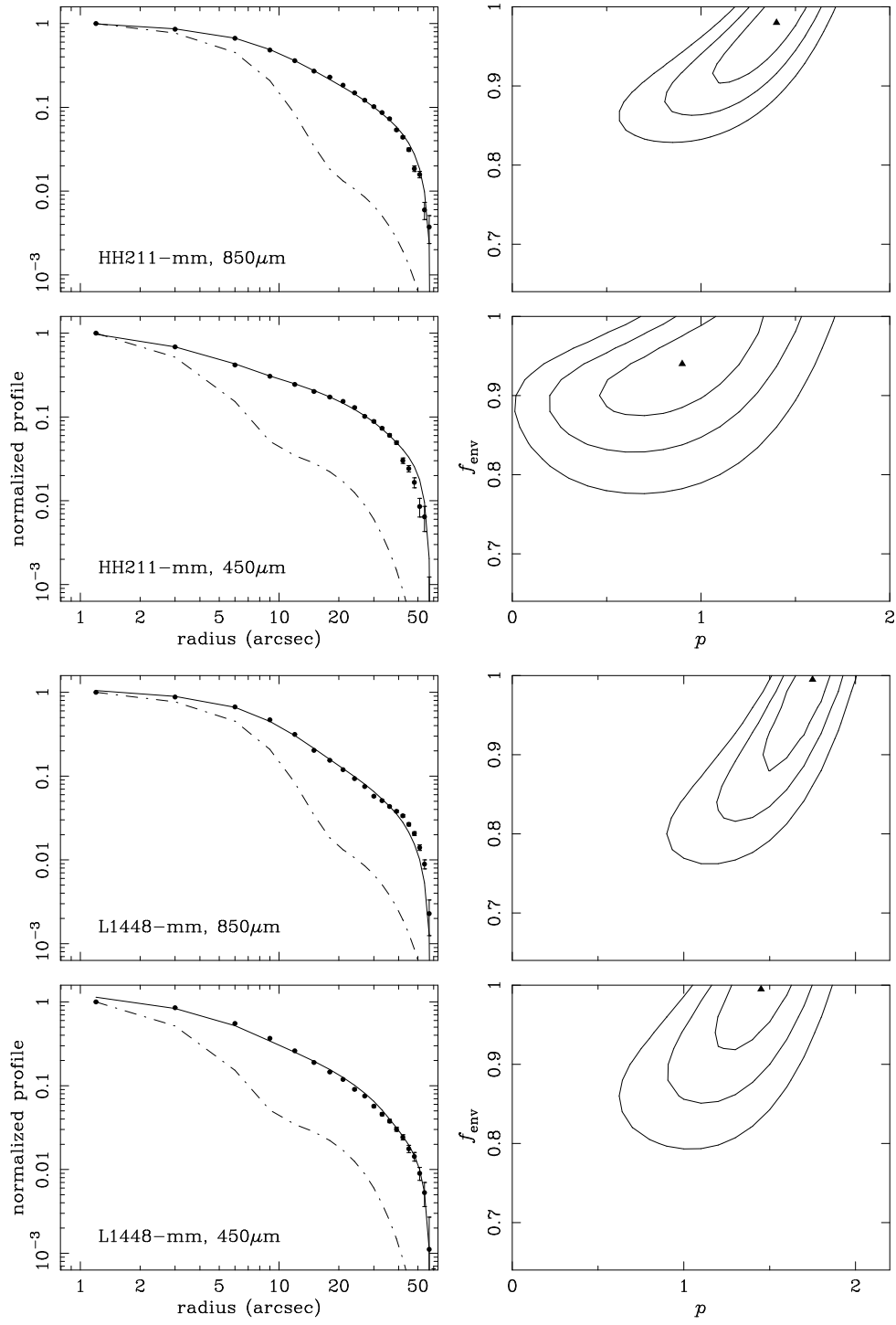


Fig. 4 (cont).

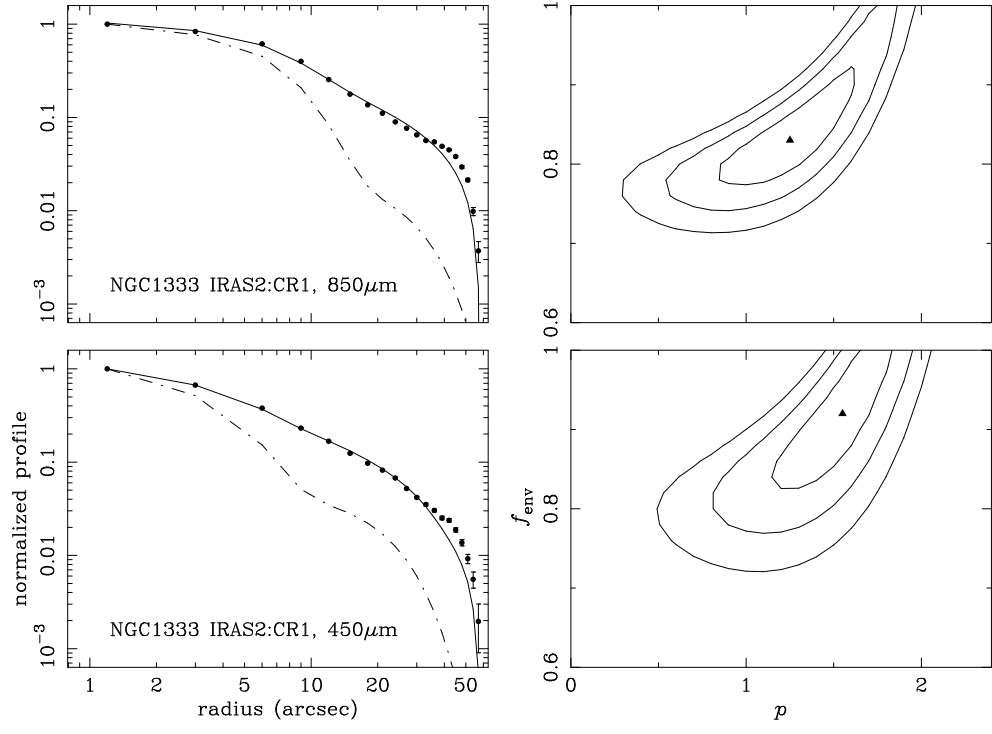


Fig. 4 (cont).

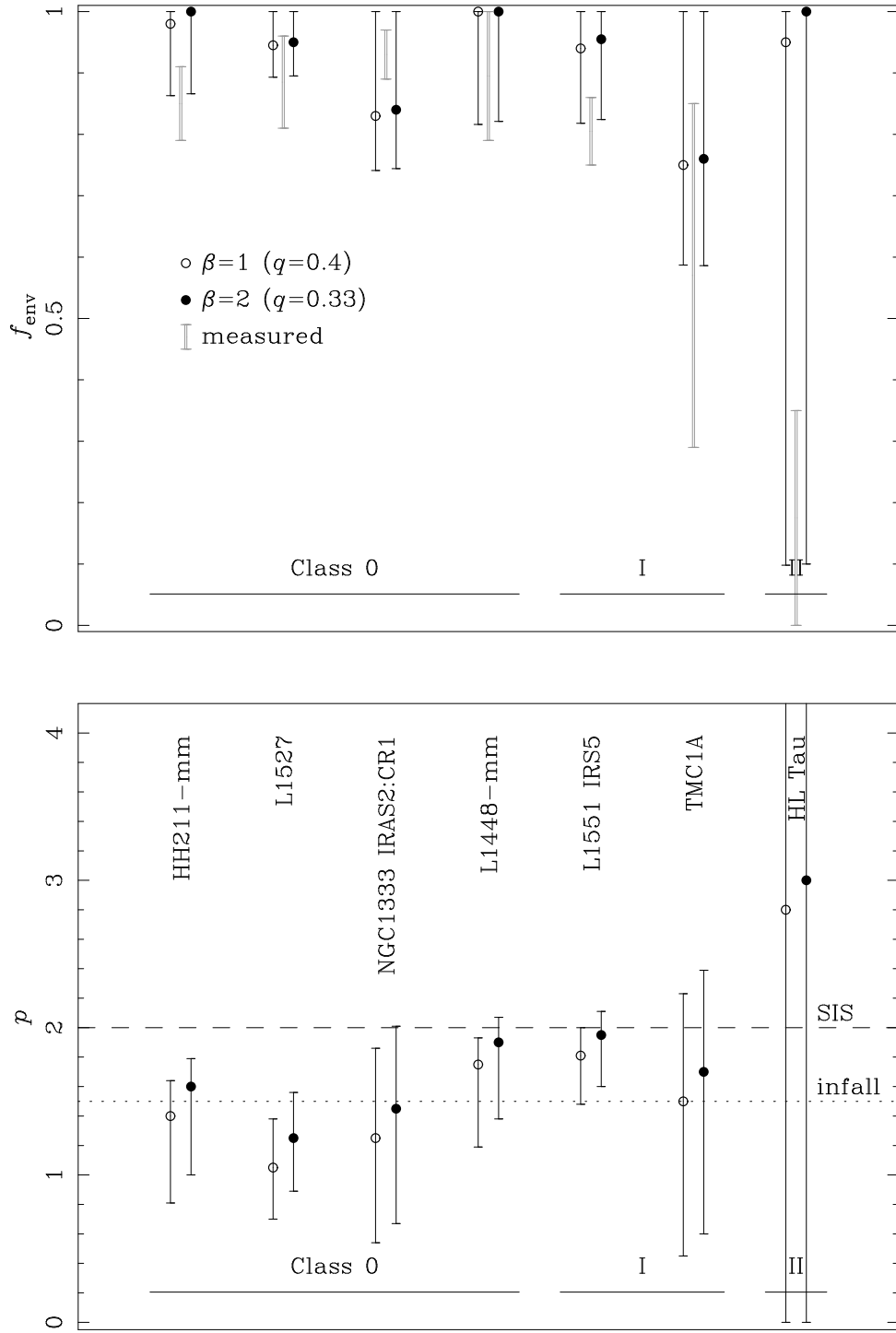


Fig. 5.

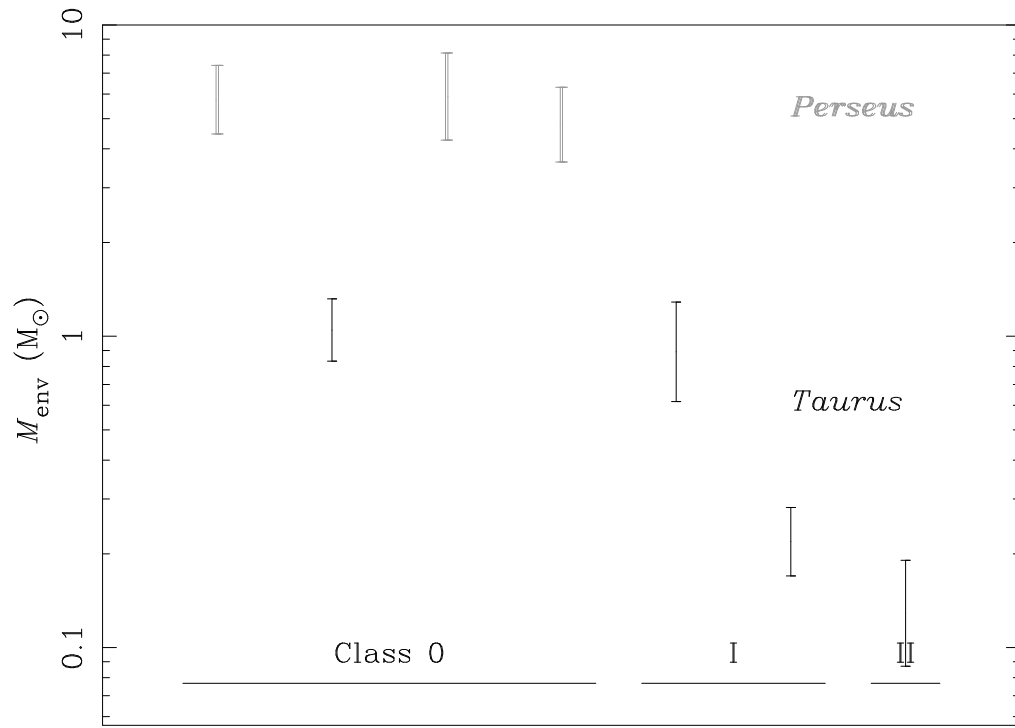


Fig. 6.

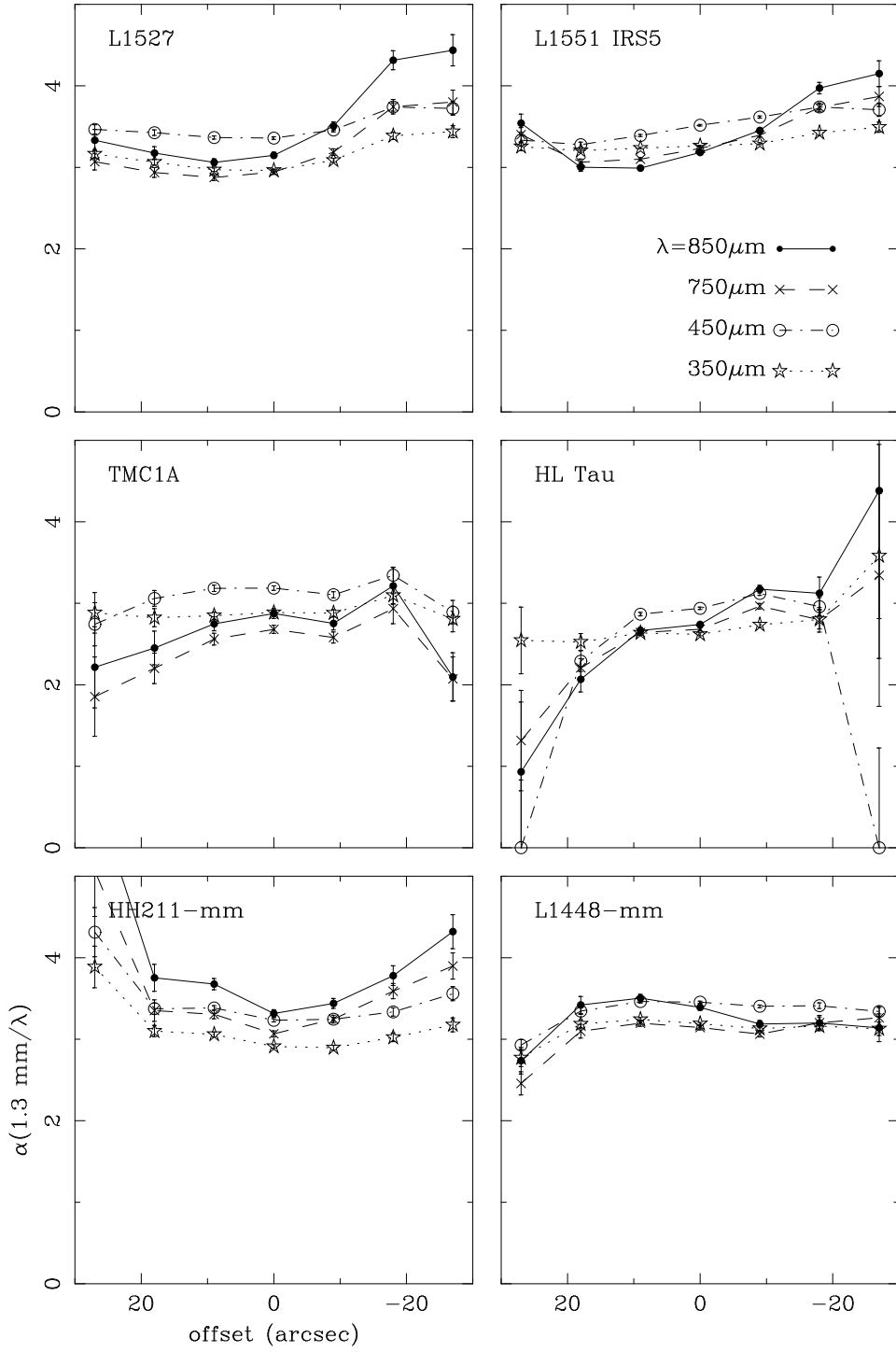


Fig. 7.

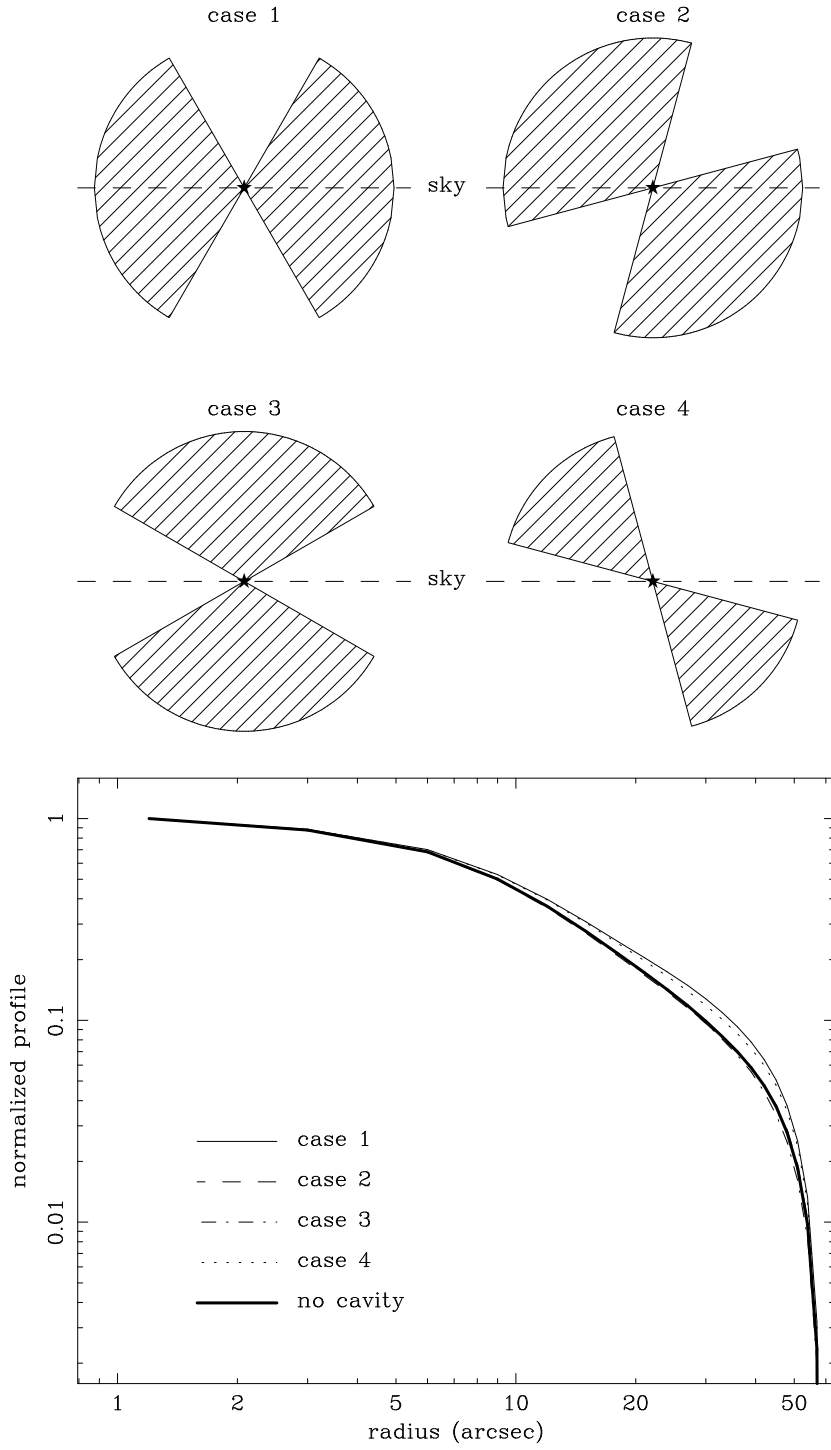


Fig. 8.

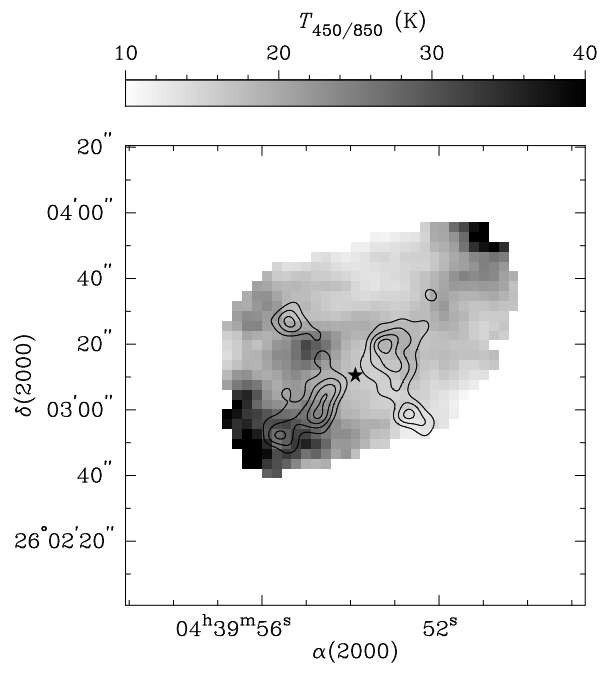


Fig. 9.

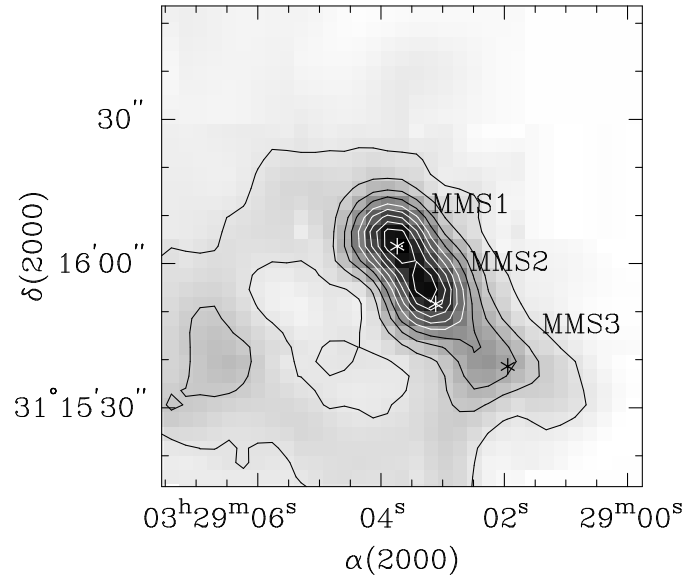


Fig. 10.